Renewable Energy 244 (2025) 122760

Contents lists available at ScienceDirect

Renewable Energy

journal homepage: www.elsevier.com/locate/renene

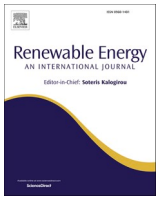

Dual-combustion chamber cycle utilizing biomass and geothermal energy: A comprehensive economic analysis and multi-objective optimization for enhanced multi-generation

Shayan Rabet [a], S.M.S. Mahmoudi [a,*], Mortaza Yari [a], Saeed Soltani [b,**]

[a] Faculty of Mechanical Engineering, University of Tabriz, 16471, Tabriz, Iran
[b] Faculty of Engineering and Natural Sciences, Antalya Bilim University, 07190, Antalya, Turkey

ARTICLE INFO

Keywords:
Digestion
Gasification
MED (multi-effect desalination)
OFC (organic flash cycle)
Multi-generation system
Multi-objective optimization

ABSTRACT

This paper proposes a novel multi-generation system comprising a digester, a gasifier, a geothermal unit, a Kalina cycle, a multi-effect desalination, a flash desalination, and an organic flash cycle. Energy, exergy, and exergo-economic analyses are performed for the system, yielding a second law efficiency of 31.97 %, total power generation of 5416 kW, a heating rate of 584.6 kW, cooling rate of 25.34 kW, freshwater production of 72.36 kg/s, and total exergy destruction of 12,273.44 kW. The highest exergy destruction occurs in the multi-effect desalination subsystem at 4546 kW (37 % of the total), followed by the digester at 2798.26 kW (22.9 % of the total). The unit exergy cost of the system products is calculated as $31.88/GJ. With a freshwater price of $1.5/m^3 and an electricity price of $ 0.14/kWh, the payback period is obtained as 5.44 years. Using the Gray Wolf algorithm, multi-objective optimizations are performed for two scenarios resulting in optimal values for the first scenario with 33.54 % second law efficiency, 6538 kW power generation, and 75.56 kg/s freshwater production. For the second scenario, the second law efficiency is 33.96 %, with a power output of 6398 kW and a total unit exergy cost of the products amounting to $33.59/GJ.

Nomenclature:

Symbols and abbreviations			
A	Area [m^2]	P	Pressure [kPa]
AI	Annual Income [$]	PCC	Post combustion chamber
AP	Air Preheater	PEC	Purchase Equipment Cost
AS	Annual saving [$]	PP	Payback Period [year]
B	Brined water [kg /s]	PRC	Pressure ratio
BPE	Boiling Point Elevation	Q	Heat transfer rate [kW]
CC	Combustion Chamber	Ri	Real Inerest rate [%]
CETD	Cold end temperature difference [K]	s	Specific entropy [kJ/kg. K]
CI	Cost index	Sep	Seperator
Cond	Condenser	SV	Seperation Vessel
CRF	Capital recovery factor	T	Temperature [K]
CV	Control volume	U	Heat transfer coefficient
D	Diameter [m]/Distilled water [kg /s]	$\dot{W}$	Power or work [kW]
DWH	Domestic Water Heater	x	Molar fraction
		Z	Height [m]

(*continued on next page*)

* Corresponding author.
** Corresponding author.
E-mail addresses: shayan.rabet2000@gmail.com (S. Rabet), s_mahmoudi@tabrizu.ac.ir (S.M.S. Mahmoudi), myari@tabrizu.ac.ir (M. Yari), soltani929@gmail.com, saeed.soltani@antalya.edu.tr (S. Soltani).

https://doi.org/10.1016/j.renene.2025.122760
Received 19 November 2024; Received in revised form 12 February 2025; Accepted 24 February 2025
Available online 24 February 2025

(*continued*)

EES	Engineering equation solver	$\dot{Z}$	Investment cost rate [$/year]
EV	Expansion Valve	**Greek symbols**	
Eva	Evaporator	η_{en}	Efficiency of energy [%]
$\dot{E}x$	Exergy rate [kW]	ε *or* η_{II}	Efficiency of exergy [%]
$\dot{E}x_D$	Exergy destruction rate [kW]	ε_{AP}	Effectiveness factor [%]
F	Feed saline water [kg /s]	ϕ	Maintenance factor
FD	Flash Desalination	**Subscripts**	
FC	Fixed Cost	0	Reference condition
FW	Freshwater	ch	Chemical
HX	Heat Exchanger	Comp	Compressor
IF	Inflation rate [%]	en	Energy
h	Specific enthalpy [kJ/kg]	ex	Exergy
i_r	Interest rate	in	Inlet
LHV	Lower heating value [MJ/kg]	is	Isentropic
LMTD	Logarithmic mean temperature difference	net	Net
$\dot{m}$	Mass flow rate [kg/s]	out	Outlet
M	Molar mass [kg/mol]	ph	Physical
MED	Multi − Effect Desalination	Pump	Pump
MSW	Municipal Solid Waste	q	Heat transfer rate
MOGWO	Multi − Objective Grey Wolf Optimization	th	Thermal
n	Plant lifetime [years]		
N	Yearly operational duration [hours]		
NPV	Net Present Value [M$]		
OC	Operation Cost [$]		

1. Introduction

With the growth of population and increasing demand for energy resources, we are facing significant challenges such as air pollution and energy shortages [1]. The use of fossil fuels not only leads to high carbon dioxide emissions but also exacerbates global warming. As a result, paying attention to clean and renewable energy sources has become more critical than ever. These sources can help reduce air pollution, combat climate change, and provide a sustainable solution for future energy supply [2]. Renewable sources offer clean, reliable, and abundant energy while significantly reducing greenhouse gas emissions and dependency on finite fossil fuels. Geothermal energy, in particular, provides a constant and stable energy output, making it a valuable complement to intermittent sources like wind and solar. Embracing these renewable technologies is essential not only for mitigating climate change but also for ensuring long-term energy security and environmental sustainability for future generations [3].

Atnaw et al. [4], in a study aimed at optimizing the calorific value of syngas produced from the gasification of oil palm tree residues, used a downdraft gasifier equilibrium model. The results indicated that an oxidation zone temperature of 1000 °C, 4 % moisture content, and an equivalence ratio of 0.35 provided optimal conditions for achieving the highest syngas calorific value (4.82 MJ/m^3). Zainal et al. [5] conducted a study on a fixed-bed gasifier to investigate the gasification of biomass. The primary objective was to assess the impact of various operational parameters, including temperature, equivalence ratio, and moisture content, on the composition of the syngas produced. The findings indicated that increasing the temperature led to higher production of hydrogen and carbon monoxide, while methane production decreased. Arun et al. [6] developed a modified equilibrium model to improve the calorific value of syngas produced from biomass gasification in a downdraft fixed-bed reactor. They investigated the effects of oxygen-enriched air (21 %–50 %) and equivalence ratio (0.15–0.35) on syngas composition. The study found that increasing oxygen concentration enhanced the production of H_2 and CO and raised the syngas's calorific value. Sittisun et al. [7] studied biomass gasification in a fixed-bed reactor using oxygen-enriched air and developed a modified equilibrium model to predict combustible gas distribution. They found that increasing the oxygen content up to 50 % enhanced hydrogen, carbon monoxide, and methane concentrations, improving the gas's lower calorific value. Ozturk and Dinçer [8] evaluated a thermodynamic system that integrates solar energy and coal gasification for the simultaneous production of electricity, heating, cooling, oxygen, hydrogen, and hot water. The system consists of six subsystems: solar, hydrogen production, coal gasification, two Rankine cycles, and absorption cooling. They found significant exergy destruction in the gasifier and combustion chamber due to irreversible reactions. Ahmadi et al. [9] developed a multi-generation cycle based on biomass gasification, which includes a biomass combustor, ORC, absorption chiller, PEM electrolyzer for hydrogen production, and a domestic water heater. Their exergy analysis indicated that the system could significantly reduce CO_2 emissions, with the combustion chamber and ORC evaporator identified as the main sources of exergy destruction due to high irreversibility. Bicer and Dinçer [10] developed an innovative combined system for producing syngas, hydrogen, and electricity, featuring components like a Rankine cycle, hydrogen production unit, Brayton cycle, SAGD steam cycle, Integrated Gasification Combined Cycle, Solid Oxide Fuel Cell, underground coal gasification, and an electrolyzer. The energy and exergy efficiencies were measured at 19.6 % and 17.3 %, respectively. Khanmohammadi et al. [11] developed an integrated biomass gasification system for multi-purpose production, focusing on reducing greenhouse gas emissions. It includes a gas turbine fed by high-temperature syngas from biomass gasification, which is then mixed with cooler gas for combustion. Taheri et al. [12] developed a multi-purpose biomass-based system for electricity, cooling, and hydrogen production, integrating technologies like gas turbine cycles, Rankine cycles, and PEM electrolyzers while utilizing LNG for thermal energy. Their comprehensive analysis revealed that increasing fuel flow by 6 kg/s decreased energy efficiency by 8.5 % and raised costs by 122.8 %. Balafkandeh et al. [13] designed an innovative CCHP biogas system combining gas turbines, S-CO_2, and a LiBr-H_2O absorption chiller for utilizing syngas or biogas. Their results indicated that the purification-based system outperforms others in efficiency, unit cost, and environmental impact, achieving an exergy efficiency of 47.8 %.

The implementation of anaerobic digestion technology reduces fossil fuel consumption and environmental pollution, contributing to sustainable development and clearly reflecting its principles [14]. Anaerobic digesters provide a sustainable solution for waste management by converting animal waste into biogas and digestate while reducing pollution and health risks [14]. Wujcik et al. [14] examined the digestion process using various thermal cycle models, focusing on the breakdown of organic acids like lactic, butyric, and propionic acids.

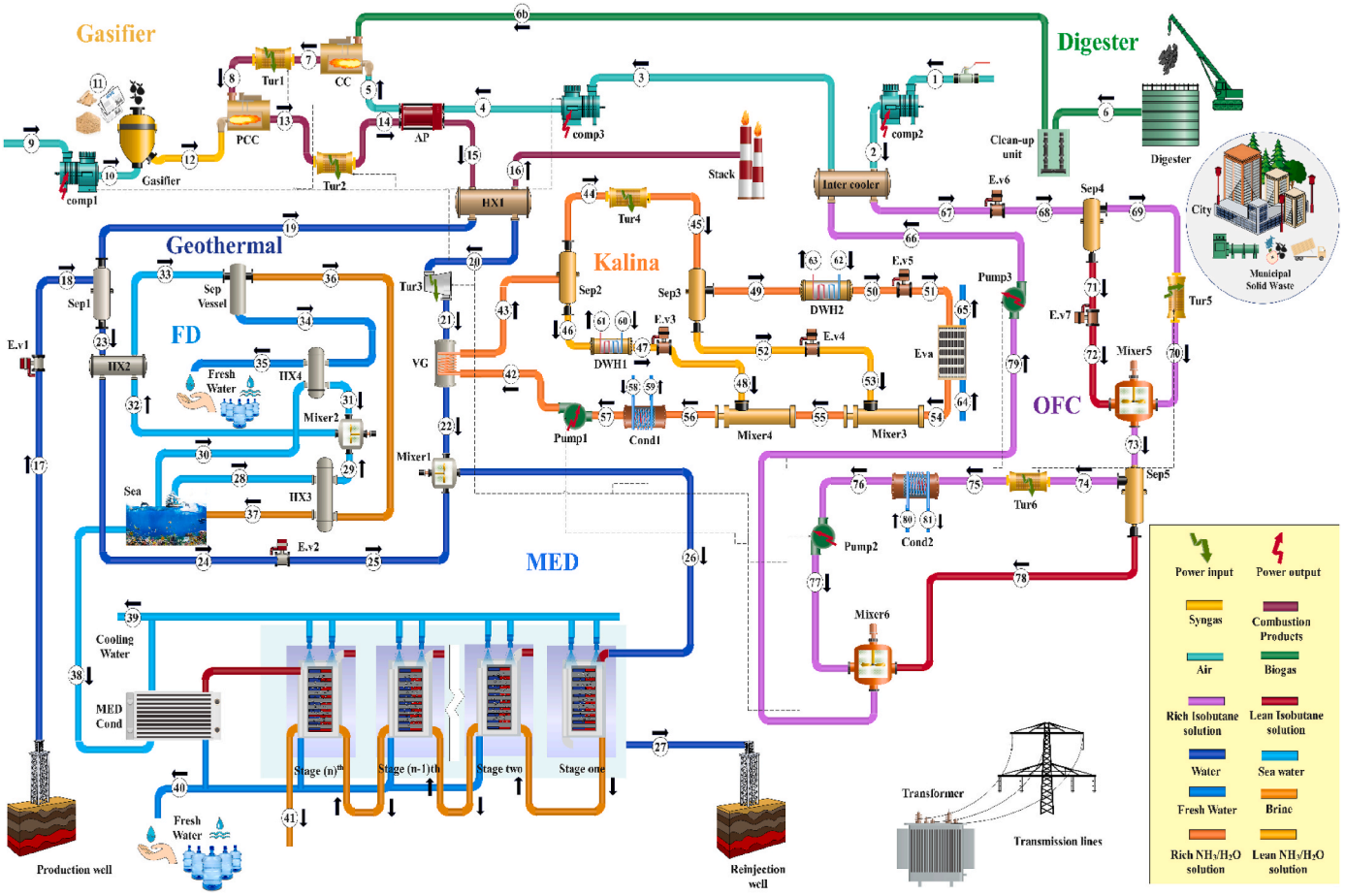

Fig. 1. Schematic overview of the proposed multi-generation system.

They found that butyric acid quickly converts to acetic acid and gas, while propionic acid decomposes without accumulating other acids. Calise et al. [15] created a dynamic simulation model for producing liquid biomethane from municipal solid waste via anaerobic digestion. The model incorporates gas upgrading and liquefaction processes alongside renewable energy sources like photovoltaic panels and solar heaters. Luo et al. [16] developed a combined heat and power system using a geothermal heat pump and anaerobic digesters for simultaneous cooling, heating, and biogas production. The integrated system achieved energy savings of 21.6 % and annual cost reductions of 35.6 % compared to separate systems. Salman et al. [17] developed a combined system integrating pyrolysis, anaerobic digestion, and a CHP plant. Municipal solid waste is converted into biochar, syngas, and bio-oil through pyrolysis, with biochar enhancing biogas production in the digester. The syngas is further converted to biomethane. This integration boosts overall system efficiency to 79.7 %, compared to 67 % for the pyrolysis-digestion combination alone. Baccioli et al. [18] examined energy recovery by integrating an ORC into a biogas plant (an anaerobic digestion facility) in Viaggio, Italy, aiming to reduce waste heat and enhance electricity production. They analyzed three ORC sizes (30, 40, and 50 kW) and found that integration significantly improved thermal energy recovery and power output.

Behzadi et al. [19] examined waste-to-energy technologies—gasification and anaerobic digestion—at a 3 MW plant in Tehran, assessing their thermodynamic, economic, and environmental impacts. They used genetic algorithms for multi-objective optimization, finding optimal exergy efficiencies of 17.98 % and 19.02 % for the two models, with associated costs of 31.28 and 27.68 $/GJ. Yari et al. [20] developed two new combined heat and power systems using solid oxide fuel cells with synthesis gas or biogas. They analyzed their thermodynamic and economic performance, revealing that the biogas-based system was more efficient for electricity production (40.14 % vs. 20.31 %). Hai et al. [21] examined a unique renewable energy system for combined heat and power, analyzing its exergy, energy, economic aspects, and CO_2 emissions. The system included a gasifier, biogas digester, multi-effect desalination, and a supercritical CO_2 cycle. They compared two biogas utilization methods: synthesis gas from the gasifier and biogas from the digester.

Mosaffa et al. [22] developed an enhanced organic flash cycle to recover geothermal energy, featuring a two-step evaporation process and a two-phase expander. Their thermal-economic assessment revealed a 36.7 % increase in net power generation with the expander and a 1.2 % boost with the two-step process, along with a slight reduction in costs. Yao et al. [23] developed a system combining flash-binary geothermal, GT, organic flash cycles, and MED for simultaneous electricity and freshwater production. Their analysis included energy, exergy, and economic evaluations, focusing on net gain and payback period. Initial results showed 37.45 % exergy efficiency, 19.02 MW power generation, and 38.69 kg/s freshwater output. Zhang et al. [24] developed a multi-output system combining geothermal, gas turbine, organic flash cycles, and multi-effect distillation for efficient electricity and freshwater production. Their analysis showed a baseline output of 8016 kW power and 15.99 kg/s freshwater, with an exergy efficiency of 35.43 % and a payback period of 3.42 years. Hamrang et al. [25] introduced a system for simultaneous electricity and freshwater production using a biogas gasifier, gas turbine, steam Rankine cycle, and multi-stage desalination. Key findings include an electricity generation of 8.347 MW, an efficiency of 46.22 %, and a freshwater output of 11.7 kg/s. Dou et al. [26] developed a hybrid system combining geothermal and biomass energy for efficient power, heating, cooling, and freshwater

production. Their system utilizes biomass combustion to enhance geothermal steam efficiency, with added subsystems like the Kalina cycle and desalination units for optimized waste heat use. The system produces 776.3 kW of power, 237 kW of heating, 15.5 kW of cooling, and 20.35 kg/s of freshwater, achieving an exergy efficiency of 19.61 %.

1.1. Principal developments and novelties

The present work presents a pioneering hybrid system making use of both a digester and a gasifier, which has been less paid attention in previous studies. The system also features two combustion chambers—the primary combustion chamber (CC) and the post-combustion chamber (PCC)—to further enhance performance.

Key innovations include.

- Dual use of digester and gasifier: Previous studies relied on either a digester or a gasifier, but this study combines both, providing flexibility for the system to use biomass and geothermal energy.
- Making use of two combustion chambers (CC and PCC): This configuration leads to more efficient combustion and energy recovery, improving the overall system performance.
- Enhanced waste heat utilization: The waste heat from the gas turbine cycle powers the Organic Flash Cycle (OFC), which boosts the efficiency of the Flash Binary Geothermal (FBG) cycle. Additionally, the waste heat runs Multi-effect Desalination (MED), Flash Desalination (FD), and Kalina cycle units to produce freshwater and meet heating and cooling demands.
- Kalina cycle for heating and cooling: Besides freshwater, the Kalina cycle is utilized to produce both heating and cooling, contributing to the system's multifunctionality.
- Reduced environmental emissions: By efficiently utilizing biomass and geothermal energy, the system significantly reduces environmental emissions, promoting sustainability.
- Comprehensive 3E (energy, exergy, and economy) analysis: A detailed 3E analysis is performed to provide a holistic evaluation of the system's performance, exceeding the scope of earlier studies.
- MOGWO optimization algorithm: The MOGWO algorithm is used to optimize the system's exergy efficiency, improving overall effectiveness and performance.
- Sensitivity analysis: The study investigates how heat recovery-based parameter variations affect system performance and production rates, providing key insights into system flexibility and efficiency.
- Net Present Value (NPV) estimation: The NPV of the system is calculated for four different electricity sale prices, offering valuable insights into its economic feasibility for potential investors.

This investigation not only fills existing gaps in previous studies but also introduces a highly efficient, multifunctional multi-generation system that can produce power, heating, cooling, and freshwater. By combining both digester and gasifier units, integrating two combustion chambers, and utilizing waste heat more effectively, this study enhances exergy efficiency while also reducing environmental emissions. The use of advanced MOGWO optimization, along with a comprehensive economic analysis, showcases the system's potential. This research can play a crucial role in the development of sustainable energy systems by improving performance both economically and environmentally.

1.2. Structure of paper

The structure of the paper is as follows:

Section 2: Provides a detailed description of the proposed poly generation system, including its components and operational framework.

Section 3: Focuses on in-depth mathematical modeling, divided into several subsections.

- Mass and Energy Analyses: Covers key performance metrics.
- Subsystem Studies: Includes analyses of the Combustion Chamber (CC), Post Combustion Chamber (PCC), Gasification unit, and Multi-Effect Desalination (MED) unit.
- Exergy Analysis: Evaluates system efficiency using the second law of thermodynamics.
- Exergoeconomic Assessment: Offers an economic evaluation linked to system efficiency.
- Multi-Objective Gray Wolf Optimization: Details the optimization process and objectives.

Section 4: Covers model validation to ensure the accuracy of the mathematical analyses.

Section 5: Discusses results, connecting analyses to the system's performance.

Section 6: Concludes with key findings and insights into the study's implications.

2. Description of the suggested system

A detailed schematic configuration for the proposed system is shown in Fig. 1 illustrating the coordination of several components for optimal energy efficiency and output. These components include.

- Digestion and Gasification Units: Biomass is utilized as a renewable energy source. Combustion products from the digestion unit react with syngas from the gasification unit in the Post Combustion Chamber (PCC), while waste heat is integrated into the geothermal power plant.
- Dual-Flash Organic Flash Cycle (OFC): Captures heat from the intercooler between the two compressors in the digestion unit, using it to generate power.
- Kalina Cycle: Enhances system performance by maximizing energy conversion efficiency and providing both heating and cooling.
- Flash Desalination (FD) and Multi-Effect Desalination (MED) Units: Improve system efficiency by producing freshwater.

The following is a summary of the primary components and their respective functions.

2.1. Digestion and gasification units

As Fig. 1 indicates, air enters compressor 2 at state 1, undergoes the first compression stage, and exits at state 2. The compressed air is cooled in the intercooler (IC) and then directed into compressor 3 for a second compression stage (state 3 to state 4). The air then enters the air preheater (AP) at state 4, absorbing thermal energy from the exhaust stream (state 5).

Simultaneously, biomass (MSW) is fed into the digester at state 6, where it undergoes moisture reduction, producing biogas, which is sent to the combustion chamber (CC). Preheated air from state 5 also enters the CC. Combustion products at state 7 move to turbine 1 (Tur1) for electricity generation, with the exhaust at state 8 directed to the post-combustion chamber (PCC).

A key innovation in this system is the use of both a gasifier and a digester. Combustion products from state 8 react with syngas from the gasifier in the PCC. Air enters compressor 1 at state 9, is compressed (state 10), and sent to the gasifier, where wood biomass (state 11) is gasified. The resulting syngas exits the gasifier at state 12 and enters the PCC to react with the combustion products.

The post-combustion products (state 13) are then sent to turbine 2 (Tur2) for power generation, exiting at state 14. The flow enters the air preheater, transferring heat to the air entering the combustion chamber, cooling down at state 15. The cooled flow passes through the first heat exchanger (HX1), transferring heat to the inlet stream before turbine 3 in the geothermal cycle, and finally exits to the stack at state 16.

Table 1
Input parameters for simulating the system.

Parameter	Value	Unit	Reference
Reference pressure, P_0	101.3	kPa	–
Reference temperature, T_0	25	$^\circ C$	–
Pressure ratio of compressors, PR_{comp}	12	–	[24]
Pressure ratio of pumps, PR_{pump}	12	–	[24]
Isentropic efficiency of turbines, $\eta_{is,Tur}$	85	%	[26]
Isentropic efficiency of compressors, $\eta_{is,Comp}$	85	%	[26]
Isentropic efficiency of pumps, $\eta_{is,Pump}$	85	%	[26]
Digestion temperature, T_6	55	$^\circ C$	[26]
Combustion temperature, T_7	1500	K	[26,30]
Post-combustion temperature, T_{13}	1350	K	[26,30]
Effectiveness of AP, ε_{AP}	60	%	[26]
Cold end temperature difference of HX1, $CETD_{HX1}$	60	K	[24,26]
Cold end temperature difference of VG, $CETD_{VG}$	100	K	[24,26]
Cold end temperature difference of IC, $CETD_{IC}$	50	K	[24,26]
Exit temperature of Air preheater, T_5	850	K	[26]
T_{17}	180	$^\circ C$	[26]
P_{17}	15	bar	[26]
MED inlet feedwater temperature, T_{39}	46	$^\circ C$	[26]
Seawater temperature, T_{38}	30	$^\circ C$	[26]
Number of MED effects, n	6	–	[26]
Salinity of seawater, x_{sw}	42	g/kg	[26]
Brine salinity, x_B	70	g/kg	[26]
Separation vessel inlet seawater temperature, T_{SV}	80	$^\circ C$	[26]
Biomass moisture content by mass for wood gasifier, MC_{Gas}	20	%	[30]
Gasification temperature, T_{12}	1073	K	[30]
Biomass temperature, T_{fuel}	298.15	K	[30]
Input data for economic analysis			
Plant expected life, bl	20	$year$	[26]
Annual number of hours, N	7000	$hour$	[26]
Maintenance factor, ϕ_r	1.06	–	[26]
Interest rate, i	15	%	[26]
Geothermal price, c_{17}	3.1	$\$/GJ$	[26]
Digestion fuel price, $c_{biomass}$	11	$\$/GJ$	[31]
Gasification fuel price, c_{11}	11	$\$/GJ$	[31]
Freshwater price, c_{fw}	1.5	$\$/m^3$	[26]
Heating price, c_{Heat}	0.03	$\$/kWh$	[26]
Cooling price, c_{cool}	0.03	$\$/kWh$	[26]
Electricity price, c_{elec}	0.14	$\$/kWh$	[26]

2.2. Geothermal power plant

The process begins with the extraction of geofluid via a production well. The fluid passes through E.V1 at state 17, where its vapor content increases. The two-phase geofluid then enters the separator Sep1, separating the liquid from the vapor. The liquid is directed to HX2, where it transfers heat to the FD subsystem, before flowing to E.V2 (state 25) and then to mixer 1 (Mix1). Meanwhile, the vapor fraction at state 19 is superheated in HX1 before entering Tur3 at state 20. The superheated geofluid expands across turbine 1, and generates electricity. The outlet stream at state 21 transfers heat to the Kalina cycle's generator (VG), before joining the liquid flow in mixer 1 (state 22). The combined flow is then returned to the ground via the injection well after participating in the multi-effect desalination (MED) system at states 26 and 27.

2.3. Flash desalination

In the FD subsystem, feedwater enters through two streams: stream 28 to HX3 and stream 30 to HX4, where both are preheated, states 29 and 31. The preheated streams are combined in Mix2, forming stream 32, which is sent to HX2. Here, it absorbs heat from the geofluid, making a two-phase flow at state 33. This stream is then directed to a separation vessel (SV), where it is separated into vapor, state 34, and liquid, state 36.

The vapor is sent back to HX4, where it transfers heat to incoming feedwater and condenses to generate freshwater at state 35. The heated liquid brine, state 36 is sent to HX3 for further heat transfer to preheat the supply water, after which it is discharged into the sea, state 37.

2.4. Kalina cycle

Water-ammonia solution at state 57 is compressed by Pump 1 before getting heated in the VG to become a two-phase stream which is sent to the separator, Sep2 at state 43, where the vapor and liquid components are separated. The vapor is directed to the turbine (Tur4) for electricity generation, while the liquid at state 46 transfers heat to water in the domestic water heater 1 (DWH1) before flowing to E.V3.

The stream exiting Tur4 flows to a separator Sep3. The separated vapor at state 49 transfers heat to DWH2, and continues through E.V5 to the evaporator (Eva) in a two-phase configuration, generating cooling at states 51 and 54. Meanwhile, liquid stream 52 flows through E.V4 (state 53) to mixer 3 (Mix3), where it combines with the output from the evaporator (state 54) and flows from E.V4 (state 53), forming stream 55. Stream 55 then merges with flow from E.V3 (state 48) in mixer 4 (state 56). Finally, the mixed stream (state 56) is cooled in condenser 1 (Cond1) (state 57), completing the Kalina cycle.

2.5. Organic flash cycle

The energy content of the stream exiting comp2 is utilized in the intercooler (IC) to run the OFC subsystem, which uses isobutane as a working fluid. The heated isobutane exits the IC at state 67 and is expanded through E.V6 before entering a separator Sep4. Across Sep4 the two-phase flow is separated into vapor at state 69, and liquid at state 71. The vapor generates electricity as it passes a turbine (Tur5) and exits at state 70, while the liquid enters E.V7, exits at state 72, and joins the vapor stream in mixer 5.

The mixed two-phase stream at state 73 leaves mixer 5 and enters a separator, (Sep5) which separates the flow into vapor at state 74, and liquid at state 78. The vapor generates electricity in a turbine (Tur6) and then flows to the condenser to become saturated liquid at state 76. The saturated liquid is pressurized by Pump 2 and mixed with the liquid flowing from Sep5 in mixer 6. Finally, the combined flow at state 79 enters Pump 3 to complete the cycle.

2.6. Multi-effect desalination

The Multi-Effect Desalination (MED) unit operates through multiple stages, each responsible for desalinating salt water. The process includes.

- Salt water is sprayed into each stage of the MED unit.
- In each stage, the sprayed salt water evaporates due to thermal energy from the previous stage, creating a continuous heating and evaporation sequence.
- The vapor from each stage condenses in the next stage, producing freshwater.
- The main challenge is providing steam for the first stage, which is done by using geothermal energy at state 26 to supply the required heat for the first evaporation process.
- Freshwater generated in this process is initially at a high temperature, but heat transfer from the warm distilled water to incoming feedwater in the MED condenser optimizes energy use and improves freshwater production.

For freshwater generation, the thermal energy from stream 26 serves as input for the first stage and is released at state 27. A portion of the feedwater evaporates using this heat, producing both freshwater vapor and brine. In subsequent stages, the latent heat of the desalinated water is recovered. The final freshwater is produced in stage n, while seawater, state 38, enters a condenser to absorb thermal energy. The seawater is separated into feedwater and cooling water, state 39, while distilled

water is produced (state 40) and brine is removed (state 41).

3. Mathematical modeling

The analysi was conducted by creating a simulation using Engineering Equation Solver (EES) software. Also, multi-objective optimization is carried out through MATLAB software. The analysis includes conservation of mass and energy as well as exergy and economic balances, all framed within the principles of thermodynamics.

The primary assumptions behind the modeling are enumerated in Table 1 and also elaborated upon below.

- The system operates under steady-state condition [27].
- The effects of changes in kinetic and potential energies are neglected [27].
- Pressure drop occurred only in the air preheater, being at a value of 5 % and 3 % for the outlet of the air preheater. The pressure drops in the connecting pipes are ignored.
- The incoming air to the gasifier complex from the first compressor is considered to have a molar composition of 21 % oxygen and 79 % nitrogen [28].
- The air entering the digester complex from the second and third compressors is considered to be 20.59 % oxygen, 77.48 % nitrogen, 0.30 % carbon dioxide, and 1.9 % water [18].
- All the gases in the multi-generation system follow the ideal gas behavior.
- The combustion chamber, the post-combustion chamber as well as all the heat exchangers are thermally insulated.
- In the multi-effect desalination system, it is assumed that the amount of feedwater flow is equally divided for each stage [29].

Details of the necessary input parameters for simulating the system under its fundamental operating circumstances is presented in Table 1.

3.1. Thermodynamic analysis

The principle of energy conservation, derived from the law of thermodynamics, is utilized to determine the conditions of each flow at the inlet and outlet of the CV, as expressed in the equations for mass and energy balance [32]:

$$\sum_{in}\dot{m}=\sum_{out}\dot{m} \tag{1}$$

$$\dot{Q}+\sum_{in}\dot{m}h=\sum_{out}\dot{m}h+\dot{W} \tag{2}$$

The exergy balance equation for a control volume operating under steady state is as follows [33]:

$$\sum_{Inlets}\dot{E}_i+\sum\dot{Q}_j\left(1-\frac{T_0}{T_j}\right)=\sum_{Outlets}\dot{E}_e+\dot{W}_{cv}+\dot{I}_{cv} \tag{3}$$

The total exergy of a stream, $\dot{E}$, is the sum of the physical and chemical exergies of the stream:

$$\dot{E}=\dot{E}_{ph}+\dot{E}_{ch} \tag{4}$$

Having neglected the kinetic and potential energies, the physical exergy of a stream is calculated using the following equation [34]:

$$\dot{E}_{th}=\sum\dot{m}_i[(h_i-h_0)-T_0(s_i-s_0)] \tag{5}$$

The chemical exergy of a mixture of ideal gases is calculated as [33]:

$$\dot{E}_{ch}=\dot{n}\left(\sum y_i\bar{e}_i^{ch,0}+\bar{R}T_0\sum y_i\,ln(y_i)\right) \tag{6}$$

where, y_i is the mole fraction of each species in the mixture, and $\bar{e}_i^{ch,0}$ is the standard chemical exergy of the species.

For the ammonia-water working fluid in the Kalina cycle, the chemical exergy is calculated using the following equation [34]:

$$\dot{E}_{ch}=\dot{m}\left[\left(\frac{X}{M_{NH_3}}\right)\bar{e}_{NH_3}^{ch,0}+\left(\frac{(1-X)}{M_{H_2O}}\right)\bar{e}_{H_2O}^{ch,0}\right] \tag{7}$$

Here, X is the ammonia concentration in the working fluid, M_{NH_3} is the molar mass of ammonia, and M_{H_2O} is the molar mass of water. The terms $\bar{e}_{NH_3}^{ch,0}$ and $\bar{e}_{H_2O}^{ch,0}$ represent the standard chemical exergies of ammonia and water, respectively.

Exergy efficiency is essentially quantified as the proportion of the exergy of the output or product relative to the exergy of the total fuel input [34]:

$$\varepsilon_i=\frac{\dot{E}_P}{\dot{E}_F}=1-\frac{\dot{E}_D+\dot{E}_L}{\dot{E}_F} \tag{8}$$

Here, $\dot{E}_P$ is the useful output exergy, $\dot{E}_F$ is the total input exergy, $\dot{E}_D$ is the destructed exergy and $\dot{E}_L$ is the exergy lost in other forms.

3.2. Gasification and digestion units

Chemical equilibrium model is used in the present work, assuming that all reactions are taken place in thermodynamic equilibrium. The pyrolysis products are expected to burn before exiting the gasifier and reach equilibrium in the reduction zone, so it is possible to use an equilibrium model in the downstream gasifier. The relevant reactions are as follows [35]:

$$\text{Boudouard}: C+CO_2\leftrightarrow 2CO\Delta H=+172\ MJ/kmole \tag{9}$$

$$\text{Water}-\text{gas heterogeneous}: C+H_2O\leftrightarrow CO+H_2\Delta H=+131\ MJ/kmole \tag{10}$$

$$\text{Mehane formation}: C+2H_2\leftrightarrow CH_4\Delta H=-75\ MJ/kmole \tag{11}$$

$$\text{Water}-\text{gas shift}: CO+H_2O\leftrightarrow CO_2+H_2\Delta H=-41\ MJ/kmole \tag{12}$$

Generally, the bimass gasification reaction can be presented by Ref. [35]:

$$CH_{1.5932}O_{0.5758}N_{0.0444}+wH_2O+m(O_2+3,76N_2)\rightarrow n_1H_2+n_2CO+n_3CO_2+n_4H_2O+n_5CH_4+n_6N_2 \tag{13}$$

where $CH_{1.5932}O_{0.5758}N_{0.0444}$ signifies the standard chemical formula of biomass, and w denotes the moisture content. The terms n_1, n_2, n_3, n_4, n_5 and n_6 represent the moles of the products in the chemical reaction.

Moreover, the relation for he moisture content is as follows [25]:

$$MC=\frac{mass\ of\ water}{mass\ of\ wet\ biomass}\times 100\quad ;\quad MC_{Wood}=20\% \tag{14}$$

The MC per mole of biomass is defined as [25]:

$$w=\frac{M_{biomass}MC}{18(1-MC)}\times 100 \tag{15}$$

Where $M_{biomass}$ is the molecular mass of the biomass fuel.

The input air quantity, m, and temperature for the gasifier, T_g , are assumed to be known. Therefore, six equations are required to calculate the values of n_i for sprcies H_2, CO, CO_2, H_2O, CH_4, and N_2. Four of these equations are obtained by balancing each atomic species in Equation (13), as shown below [25]:

$$\text{Carbon}: n_2 + n_3 + n_5 = 1 \tag{16}$$

$$\text{Hydrogen}: 2n_1 + 2n_4 + 4n_5 = 1,5932 + 2w \tag{17}$$

$$\text{Oxygen}: n_2 + 2n_3 + n_4 = 0,5758 + w + 2m \tag{18}$$

$$\text{Nitrogen}: 2n_6 = 3,76 \times 2m + 0,0444 \tag{19}$$

Taking into account the methane formation reaction and the shift reaction, the equilibrium constants for these reactions are determined as follows [25]:

$$K_1 = \frac{y_{CH_4}}{\left(y_{H_2}\right)^2}, \left(\frac{P_g}{P_0}\right)^{-1} = e^{-\frac{\Delta G^0_1}{RTg}} \tag{20}$$

$$K_2 = \frac{y_{CO_2} y_{H_2}}{y_{CO} y_{H_2O}}, \left(\frac{P_g}{P_0}\right)^{0} = e^{-\frac{\Delta G^0_2}{RTg}} \tag{21}$$

Where, K_1 and K_2 are the equilibrium constant of a reaction, y_{CH_4}, y_{H_2}, $y_{CO_2}, y_{H_2}, y_{H_2O}$ and y_{CO} are the mole fraction and P_g denotes the partial pressure of the gas involved in the reaction.

Changes in the standard Gibbs free energy of the respective reactions are represented by ΔG^0_1 and ΔG^0_2. Also, R represents the gas constant. The defined Gibbs free energy can be formulated as follows [36]:

$$-\Delta G^0_1 = \left[\bar{h}_{CH_4} - T_g \bar{s}^0_{CH_4}\right] - 2\left[\bar{h}_{H_2} - T_g \bar{s}^0_{H_2}\right] \tag{22}$$

$$-\Delta G^0_2 = \left[\bar{h}_{CO_2} - T_g \bar{s}^0_{CO_2}\right] + \left[\bar{h}_{H_2} - T_g \bar{s}^0_{H_2}\right] - \left[\bar{h}_{CO} - T_g \bar{s}^0_{CO}\right] - \left[\bar{h}_{H_2O} - T_g \bar{s}^0_{H_2O}\right] \tag{23}$$

Here, $\bar{h}_i$ and $\bar{s}^0_i$ are specific molar enthalpy and specific molar entropy, respectively. An energy balance is used to evaluate the gasification temperature (T_g) assuming no heat loss from the gasifier as follows [36, 37]:

$$\bar{h}^0_{f,biomass} + w\bar{h}^0_{f,H_2O} = n_1\left(\bar{h}^0_{f,H_2} + \Delta\bar{h}_{H_2}\right) + n_2\left(\bar{h}^0_{f,CO} + \Delta\bar{h}_{CO}\right) + n_3\left(\bar{h}^0_{f,CO_2} + \Delta\bar{h}_{CO_2}\right) + n_4\left(\bar{h}^0_{f,H_2O} + \Delta\bar{h}_{H_2O}\right) + n_5\left(\bar{h}^0_{f,CH_4} + \Delta\bar{h}_{CH_4}\right) + n_6\left(\bar{h}^0_{f,N_2} + \Delta\bar{h}_{N_2}\right) \tag{24}$$

Here, $\bar{h}^0_{f,biomass}$, $\bar{h}^0_{f,H_2O}$, $\bar{h}^0_{f,H_2}$, $\bar{h}^0_{f,CO}$, $\bar{h}^0_{f,CO_2}$, $\bar{h}^0_{f,H_2O}$, $\bar{h}^0_{f,CH_4}$ and $\bar{h}^0_{f,N_2}$ express the enthalpies of formation of biomass, moisture, hydrogen, carbon monoxide, water, methane and nitrogen, respectively.

The specific chemical exergy of biomass can be estimated as follows [38]:

$$e^{ch}_{biomass} = \beta LHV_{biomass} \tag{25}$$

here, the factor β represents the ratio of chemical exergy to LHV of biomass. A statistical coefficient for β is as follows:

$$\beta = \frac{1,044 + 0,016\frac{Z_H}{Z_C} - 0,34493\frac{Z_O}{Z_C}\left(1 + 0,0531\frac{Z_H}{Z_C}\right)}{1 - 0,4124\frac{Z_O}{Z_C}} \tag{26}$$

where Z_O, Z_C and Z_H are the weight fractions of oxygen, carbon and hydrogen, respectively.

For the digestion process, a thermophilic anaerobic digester operating at 55 °C was employed. To sustain microbial activity, temperature variations are disregarded. The composition of biogas is deduced solely from the organic (ash-free) fraction of Municipal Solid Waste (MSW), using the method established by Zhang et al. [24]. The universally accepted reaction for biomass digestion is as follows [39]:

$$C_nH_aO_b + wH_2O \rightarrow n_7CO_2 + n_8CH_4 \tag{27}$$

in the present work, it is assumed that 95 % of the biomass contains volatile compounds, and 70 % of these volatile substances can be decomposed and converted into biogas by anaerobic bacteria, and the rest is removed from the end of the digester as liquid manure. Due to the insignificant amount of other produced gases in the anaerobic digestion process, the effect of it has been neglected.

The molar balance for species read as [19]:

$$\text{Carbon}: (0,95 \times 0,7)n_{MSW} \times 100 = n_7 + n_8 \tag{28}$$

$$\text{Hydrogen}: (0,95 \times 0,7)n_{MSW} \times 196 + 2w = 4n_8 \tag{29}$$

$$\text{Oxygen}: (0,95 \times 0,7)n_{MSW} \times 38 + w = 2n_7 \tag{30}$$

Here, the terms n_7 and n_8 represent the moles of the products in the chemical reaction.

3.3. Multi-effect desalination unit

Temperature regulation at each stage: The operational temperatures at every stage of the MED system are essential. Considering that the system has numerous stages, the temperature differential (ΔT) between the brine flow at each stage (T) is presumed to be constant and determined as follows [26]:

$$\Delta T = \frac{(T_1 - T_n)}{n} \tag{31}$$

In this section, T_1 indicates the temperature of the salt water entering the system, T_n is the temperature of the brine exiting the last step, and n indicates the number of desalination steps. This temperature difference helps to better regulate and control the evaporation and condensation process in each stage and leads to an increase in the overall efficiency of the system.

Similarly, the temperature at each level is calculated using the subsequent equation [26]:

$$T_{i+1} = T_i + \Delta T \quad ; \quad i = 1, 2, \ldots, n \tag{32}$$

The evaporation temperature (T_v) at each stage is determined by considering the elevation in boiling point (BPE). Consequently, T_v for every stage is defined as follows [26]:

$$T_{v_n} = T_n - BPE_n \tag{33}$$

$$BPE_n = \left(8,325 \times 10^{-2} + 1,883 \times 10^{-4} \times T_n + 4,02 \times 10^{-6} \times T_n^2\right)Y_{b_i} + \left(-7,625 \times 10^{-4} + 9,02 \times 10^{-5} \times T_n - 5,2 \times 10^{-7} \times T_n^2\right)Y_{b_i}^2 + \left(1,522 \times 10^{-4} - 3 \times 10^{-6} \times T_n - 3 \times 10^{-8} \times T_n^2\right)Y_{b_i}^3 \tag{34}$$

Boiling point elevation (BPE) is due to the presence of solutes in salt water, which increases the evaporation temperature compared to pure

Table 2
The range of decision variables in the gray wolf algorithm method.

Decision variable	Unit	Lower bound	Upper bound
Cold − end temperature diffrence $_{IC}$	K	44	56
Cold − end temperature difference$_{VG}$	K	70	130
Cold − end temperature difference$_{HX1}$	K	40	80
Pressure ratio of turbines and compressors	–	3	12
The saline feedwater temperature, T_f	$^{\circ}C$	40	46
The inlet air temperature to the combustion chamber, T_5	K	835	870

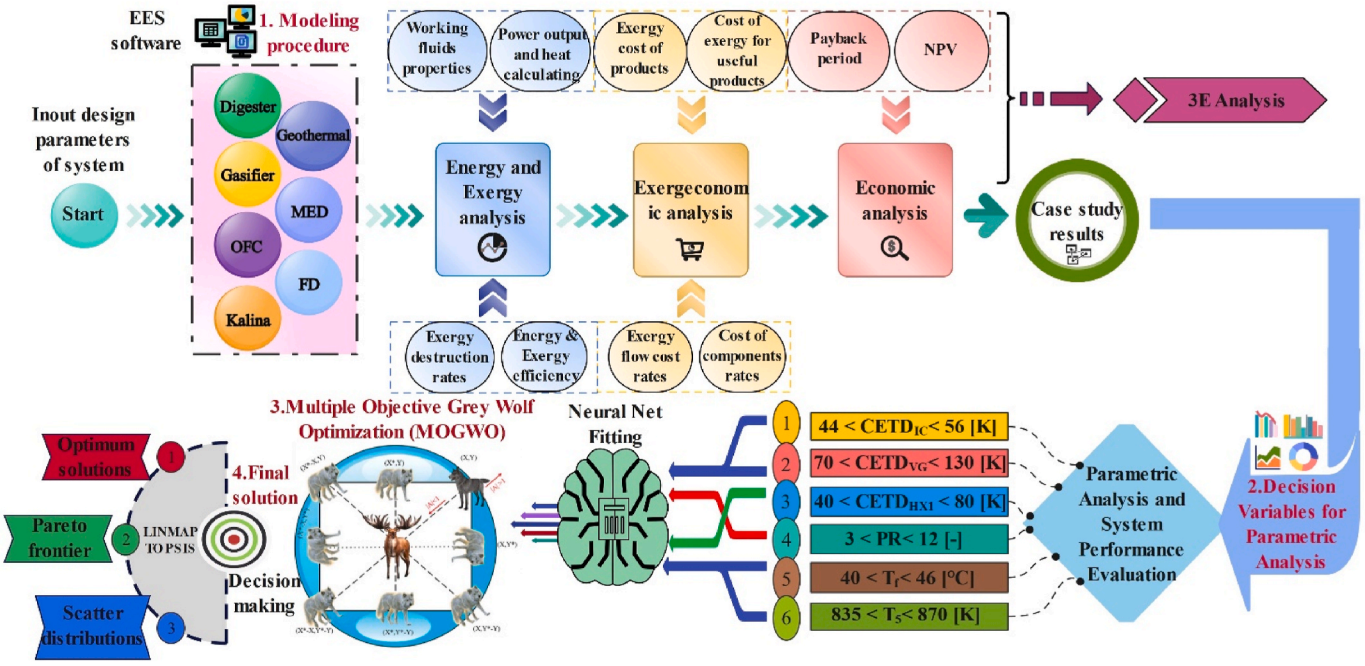

Fig. 2. Comprehensive modeling and optimization methodology.

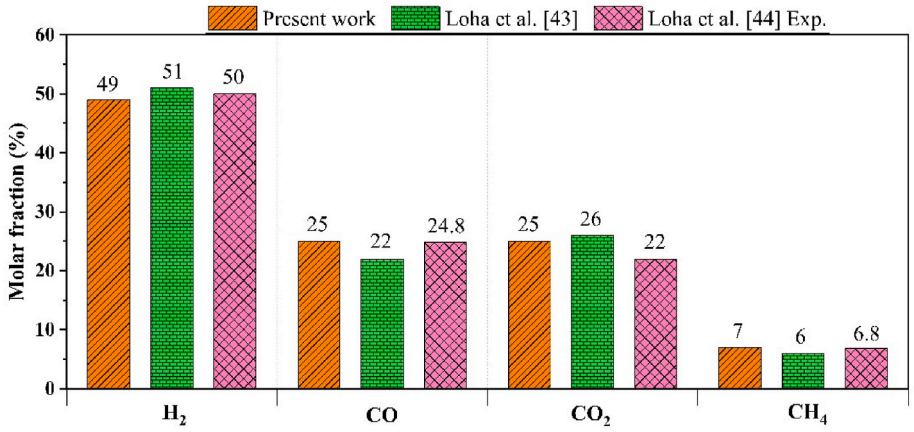

Fig. 3. Validation of the gasifier by comparing the mole fraction of combustion products with the paper of Loha et al. [43,44].

Table 3
Model validation of the Kalina cycle [45].

Variable	Present study	Reference	Relative difference (%)
Power output (kW)	199.440	199.442	0.001
Energy efficiency (%)	8.312	8.310	0.024
Exergy efficiency (%)	31.261	31.260	0.003

Table 4
Model validation of the MED with the paper of Abdelhay et al. [40].

Variable	Present study	Reference	Relative difference (%)
Feedwater flow rate (kg/s)	12.73	12.7315	0.01
Brine flow rate (kg/s)	6.366	6.36574	0.01
Incoming seawater flow rate (kg/s)	46.11	45.8412	0.58
Cooling water flow rate (kg/s)	33.38	33.1097	0.8
First stage temperature (°C)	65.22	65.2222	0
Final stage temperature (°C)	38.78	38.7778	0
Area of MED (m^2)	1894	1864.81	1.54
Heating stream flow rate (kg/s)	1.096	1.17406	6.75
GOR (−)	5.81	5.42199	6.71
SHTA (m^2/kg/s)	297.5	292.945	1.53

water.

The assessment of brine (B): The calculation of seawater flow in the first stage differs from that in subsequent stages. In the first stage [26]:

$$B_1 = F_1 - D_1 \tag{35}$$

in this context, F denotes the feedwater rate, whereas D signifies the freshwater flow rate. The freshwater flow rate in the first stage is ascertained as follows [26]:

$$D_1 = \left(D_0\left(h_d - h_{fd}\right) - F_1 C_p (T_1 - T_F)\right) / \lambda_1 \tag{36}$$

$$\lambda_1 = 2501,897149 - 2,407064037 \times T_i + 1,192217 \times 0,001 \times T_i^2 - 1,5863 \times 10^{-5} \times T_i^3 \tag{37}$$

The equation outlines the energy balance for the first stage of the Multi-Effect Distillation (MED) system, incorporating variables such as D_1 (freshwater flow rate), D_0 (steam flow rate), h_d (steam enthalpy), h_{fd} (feed enthalpy), F_1 (feed flow rate), C_p (specific heat capacity of saltwater), T_1 (temperature of the first stage), T_F (incoming feedwater temperature), and λ_1 (latent heat of evaporation).

Estimation of salt content in saline water: The salinity of saline water is firstly assessed as follows [26]:

$$Y_{b_1} = F_1 Y_{F_1} / B_1 \tag{38}$$

In this context, F denotes the feedwater rate, Y_{F_1} is the salt concentration of the saline water at flow.

The flow rate of freshwater produced in the first stage is calculated as:

$$D_1 = \left(\left(\dot{m}_{17}(h_{26} - h_{27})\right) - F_1 C_p (T_1 - T_F)\right) / \lambda_1 \tag{39}$$

Here, D_1 denotes freshwater flow rate, D_0 is steam flow rate, F_1 (feed flow rate), C_p (specific heat capacity of saltwater), T_1 (temperature of the first stage), T_F (incoming feedwater temperature), and λ_1 (latent heat of evaporation).

The flow rate of produced freshwater for the next steps is determined as [26]:

$$D_i = \left((D_{i-1})\lambda_{i-1} - F_i C_p (T_i - T_F) + B_{i-1} C_p (T_{i-1} - T_i)\right) / \lambda_1 \tag{40}$$

The flow rate of brine for the next steps is determined as follows [26]:

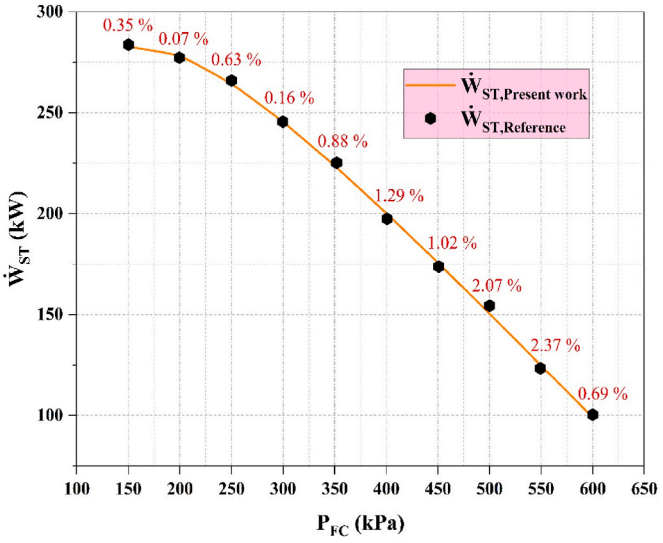

Fig. 4. Validation of geothermal power plant [47].

Table 5
Validation of one for geothermal power plant with the paper of Yari [46].

State no.	Pressure P (KPa)	Present work Temperature T (°C)	Mass flow rate $\dot{m}\left(\frac{Kg}{s}\right)$	Ref [46] Mass flow rate $\dot{m}\left(\frac{Kg}{s}\right)$	Error (%)	Enthalpy $h\left(\frac{KJ}{Kg}\right)$	Ref [46] Enthalpy $h\left(\frac{KJ}{Kg}\right)$	Error (%)	Entropy $s\left(\frac{KJ}{KgK}\right)$	Ref [46] Entropy $s\left(\frac{KJ}{KgK}\right)$	Error (%)
1	2795	230	1	1	0.00	990.1	990	−0.01	2.61	2.61	0.00
2	666.5	163	1	1	0.00	990.1	990	−0.01	2.664	2.664	0.00
3	666.5	163	0.1456	0.1454	−0.13	2761	2761	0.00	6.725	6.725	0.00
4	96.4	98.58	0.1456	0.1454	−0.13	2531	2531	0.00	6.988	6.99	0.02
5	96.4	98.58	0.2496	0.2496	0.00	2590	2591	0.0386	7.148	7.149	0.01
6	7.381	39.99	0.2496	0.2496	0.00	2336	2336	0.00	7.496	7.498	0.02
7	7.381	39.99	0.2496	0.2496	0.00	167.5	167.5	0.00	0.5723	0.5723	0.00
8	666.5	163	0.8544	0.8546	0.023	688.4	688.7	0.0436	1.972	1.973	0.05
9	96.4	98.58	0.8544	0.8546	0.023	688.4	688.7	0.0436	2.032	2.032	0.00
10	96.4	98.58	0.104	0.1042	0.192	2673	2673	0.00	7.371	7.372	0.01
11	96.4	98.58	0.7504	0.7504	0.00	413.2	413.1	−0.024	1.291	1.291	0.00
12	100	25	53.86	53.86	0.00	298.6	298.6	0.00	5.699	5.699	0.00
13	100	35	53.86	53.86	0.00	308.6	308.6	0.00	5.733	5.732	−0.01

Table 6
Validation of a geothermal power plant, comparison of the efficiency of Singh's first law and double flash with the paper of Yari [46].

	Single-flash			Double-flash		
Performance parameters	Present study	Reference [46]	Error (%)	Present study	Reference [46]	Error (%)
η_I (%)	8.58	8.577	0.034	10.7	10.95	2.34

Table 7
The states provide information pertaining to the present work.

State	Working fluid	T [°C]	P [kPa]	ṁ [kg /s]	Concentration	Ėx [kW]	c [$/GJ]
1	Air	25	101.3	6.795	–	0	0
2	Air	172.6	350.9	6.795	–	924.4	33.6
3	Air	96.68	350.9	6.795	–	782.4	33.6
4	Air	276.6	1216	6.795	–	1951	32.83
5	Air	576.9	1155	6.795	–	3190	33.14
6	Biomass	55	1216	0.3	–	6334	12.31
7	Combustion Products	1227	1097	7.095	–	7705	24.01
8	Combustion Products	912.1	316.7	7.095	–	4719	24.01
9	Air	25	101.3	0.2026	–	0	0
10	Air	173.1	350.9	0.2026	–	27.39	33.61
11	Biomass	25	350.9	0.1262	–	1970	11
12	Syngas	800	350.9	0.3288	–	1797	15.64
13	Combustion Products	1077	300.9	7.424	–	6197	22.91
14	Combustion Products	798.2	104.4	7.424	–	3534	22.91
15	Combustion Products	550.4	101.3	7.424	–	1986	22.91
16	Combustion Products	211.8	101.3	7.424	–	454.7	22.91
17	Water	180	1500	115.5	–	15337	3.1
18	Water	151.8	500	115.5	–	14931	3.239
19	Water	151.8	500	6.753	–	4873	3.239
20	Water	351.8	500	6.753	–	6084	8.412
21	Water	184.7	100	6.753	–	3616	8.412
22	Water	132.9	100	6.753	–	3402	8.412
23	Water	151.8	500	108.8	–	10059	3.239
24	Water	110	500	108.8	–	4982	3.239
25	Water	99.61	100	108.8	–	4893	3.456
26	Water	99.61	100	115.5	–	8280	5.499
27	Water	69.61	100	115.5	–	1756	5.499
28	Seawater	25	101.3	105.9	42	0.1337	0
29	Seawater	45	101.3	105.9	42	265.6	42.28
30	Seawater	25	101.3	173.9	42	0.2195	0
31	Seawater	44.09	101.3	173.9	42	397.5	48.02
32	Seawater	44.44	101.3	279.8	42	662.8	45.75
33	Seawater	80	101.3	279.8	42	5037	10.43
34	Water	69.09	30	5.641	–	1781	10.31
35	Water	69.09	30	5.641	–	83.8	10.31
36	Brine	69.65	101.3	274.1	42.86	3315	10.31
37	Brine	62.36	101.3	274.1	42.86	2350	10.31
38	Seawater	30	101.3	410.1	42	57.44	0
39	Seawater	46	101.3	243.3	42	672.8	0
40	Water	69.3	30.27	66.72	–	998.5	43.97
41	Brine	47.19	101.3	100.1	70	363.2	0
42	NH_3H_2O	32.9	1000	0.493	0.28	2730	14.2
43	NH_3H_2O	155	1000	0.493	0.28	2897	14.08
44	NH_3H_2O	155	1000	0.2386	0.4795	2383	14.08
45	NH_3H_2O	141.3	700	0.2386	0.4795	2368	14.08
46	NH_3H_2O	155	1000	0.2543	0.09285	513.7	14.08
47	NH_3H_2O	85	1000	0.2543	0.09285	495.2	14.08
48	NH_3H_2O	75.46	100	0.2543	0.09285	494.9	14.09
49	NH_3H_2O	141.3	700	0.2342	0.487	2359	14.08
50	NH_3H_2O	53.07	700	0.2342	0.487	2249	14.08
51	NH_3H_2O	9.234	100	0.2342	0.487	2245	14.11
52	NH_3H_2O	141.3	700	0.004482	0.08659	8.435	14.08
53	NH_3H_2O	85.75	100	0.004482	0.08659	8.359	14.21
54	NH_3H_2O	15	100	0.2342	0.487	2244	14.11
55	NH_3H_2O	16.48	100	0.2386	0.4795	2252	14.11
56	NH_3H_2O	47.08	100	0.493	0.28	2736	14.16
57	NH_3H_2O	32.81	100	0.493	0.28	2730	14.16
58	Water	25	101.3	2.908	–	7.263	0
59	Water	35	101.3	2.908	–	9.257	31.35
60	Water	25	101.3	0.5263	–	1.315	0
61	Water	60	101.3	0.5263	–	5.51	55.41
62	Water	25	101.3	3.469	–	8.665	0
63	Water	60	101.3	3.469	–	36.32	47.48
64	Water	20	101.3	0.6049	–	1.618	0
65	Water	10	101.3	0.6049	–	2.501	81.7
66	Isobutane	46.68	3500	1.927	–	111	106.3
67	Isobutane	131.9	3500	1.927	–	209.6	80
68	Isobutane	100.4	2000	1.927	–	195.5	85.84
69	Isobutane	100.4	2000	1.132	–	134.7	85.84
70	Isobutane	72.54	1000	1.132	–	105.7	85.84
71	Isobutane	100.4	2000	0.7946	–	60.84	85.84
72	Isobutane	66.23	1000	0.7946	–	55.97	93.4
73	Isobutane	66.23	1000	1.927	–	161.6	88.53
74	Isobutane	66.23	1000	1.483	–	135.7	88.53

(*continued on next page*)

Table 7 (*continued*)

State	Working fluid	T [°C]	P [kPa]	ṁ [kg /s]	Concentration	Ėx [kW]	c [$/GJ]
75	Isobutane	44.61	500	1.483	–	95.67	88.53
76	Isobutane	37.74	500	1.483	–	75.59	88.53
77	Isobutane	38.1	1000	1.483	–	76.99	91.93
78	Isobutane	66.23	1000	0.4445	–	25.84	88.53
79	Isobutane	44.81	1000	1.927	–	101.8	92
80	Water	25	101.3	23.22	–	58.01	0
81	Water	30	101.3	23.22	–	62.04	34.77

$$B_i = B_{i-1} + F_i - D_i = (B_{i-1} + F_{i-1} - D_{i-1}) + F_i - D_i = \sum_{k=1}^{i} F_k - D_k \tag{41}$$

The salt concentration of the brine for the next steps is determined as [26]:

$$Y_{b_i} = \left(Y_F F_i + Y_{b_{i-1}} B_{i-1}\right) / B_i \tag{42}$$

Here, F denotes the feedwater rate, Y_F is the salt concentration of the saline water at flow.

Freshwater production rate in MED unit is calculated as follows [26]:

$$\dot{m}_{fw} = \sum_{i=1}^{n} D_i \tag{43}$$

Required heating steam flow rate: The required heating steam flow rate for the multi-effect desalination system is calculated using the energy balance [40]:

$$\dot{M}_{HS} \times \left(h_{ms,in} - h_{ms,out}\right) = F_1 \times c_p \times (T_1 - T_F) + D_1 \times LH_1 + B_1 \times c_p \times T_1 \tag{44}$$

where, $\dot{M}_{HS}$ indicates the heating steam flow rate, $h_{ms,in}$ indicates the enthalpy of steam entering the system, $h_{ms,out}$ indicates the enthalpy of steam leaving the system, and LH_1 represents the latent heat of evaporation at the temperature of evaporation of salt water in the first stage.

To calculate the areas, the heat transfer coefficient is first obtained from the following equation [29]:

$$U_i = \frac{\left(1939,4 + 1,40562 \times T_i - 0,0207525 \times (T_i)^2 + 0,0023186 \times (T_i)^3\right)}{1000} \tag{45}$$

The heat transfer area for the first stage of the multi-effect desalination system is calculated as [29]:

$$A_1 = \frac{\dot{m}_{26} \times \lambda_1}{U_1 \times (T_{26} - T_1)} \tag{46}$$

Here, λ_1 is latent heat of evaporation and T_1 denotes the temperature of first stage.

The heat transfer area for stages 2 to n in the multi-effect desalination system can be calculated as follows [29]:

$$A_i = \frac{D_i \times \lambda_i}{U_i \times (T_{i-1} - T_i)}, i = 2, 3, 4, \ldots, n \tag{47}$$

In this context, D_i denotes freshwater flow rate and λ_i is latent heat of evaporation.

The total heat transfer area of the steps (A_e) is given by the following equation [29]:

$$A_e = A_1 + A_2 + A_3 + \ldots + A_n = \sum_{i=1}^{n} A_i \tag{48}$$

The logarithmic mean temperature difference and the overall heat transfer coefficient for the condenser are obtained using the following two equations [29]:

$$LMTD_c = \frac{(T_F - T_{cw})}{ln\left[\frac{T_{v_n} - T_{cw}}{T_{cn} - T_F}\right]}, T_{c_n} = T_n - BPE_n \tag{49}$$

$$U_c = 1,7194 + 3,2063 \times 10^{-2} \times T_{v_n} - 1,5971 \times 10^{-5} \times (T_{v_n})^2 + 1,9918 \times 10^{-7} \times (T_{v_n})^3 \tag{50}$$

Here, T_{v_n} is evaporation temperature, T_F denotes feedwater temperature and BPE_n is boiling point elevation in every stage.

The heat transfer area of the condenser is obtained as [29]:

$$A_c = \frac{D_n \times \lambda_n}{U_c \times LMTD_c} \tag{51}$$

The total area of the desalination plant is obtained from the following equation [29]:

$$A_{tot,MED} = A_e + A_c \tag{52}$$

Table S1 of supplementary file [33] illustrates the application of these thermodynamic methods to the equipments of the system for enhanced comprehension.

3.4. Exergoecomic assessment

For the exergy-economic analysis in the present work the SPECO method is used. The cost balance for each system component is outlined accordingly [33]:

$$\sum \dot{C}_{out,k} + \dot{C}_{W,k} = \sum \dot{C}_{in,k} + \dot{C}_{Q,k} + \dot{Z}_k \tag{53}$$

Here, $\dot{C}$ is the cost rate, $\dot{Z}$ is the cost rate related to the capital investment plus the operation and maintenance cost rate related to each system component [33]:

$$\dot{Z}_k = Z_k^{CI} + Z_k^{OM} \tag{54}$$

To calculate the value of $\dot{Z}_k$ based on the purchase equipment cost (PEC) as available data, the following relationship can be used [33]:

$$\dot{Z}_k = Z_k^{CI} + Z_k^{OM} = CRF \times TCI_k \times \left(\frac{24 \times 365}{N}\right) + \phi_r \times PEC_k \tag{55}$$

In the above relationship, CRF is the capital recovery factor, N is the number of annual operating hours of the system, bl is the useful life of the system, i the interest rate, and the term ϕ_r also shows the repair factor [33].

$$CRF = \frac{i(1+i)^{bl}}{i(1+i)^{bl} - 1} \tag{56}$$

Finally, purchase equipment costs are updated to the current year using the CEPCI [33]:

$$PEC_k = PEC \times \frac{CEPCI_{2022}}{CEPCI_{orginal}} \tag{57}$$

the cost index for 2020 is 813 [25].

The relative cost difference (r_k) and the exergy-economic factor (f_k)

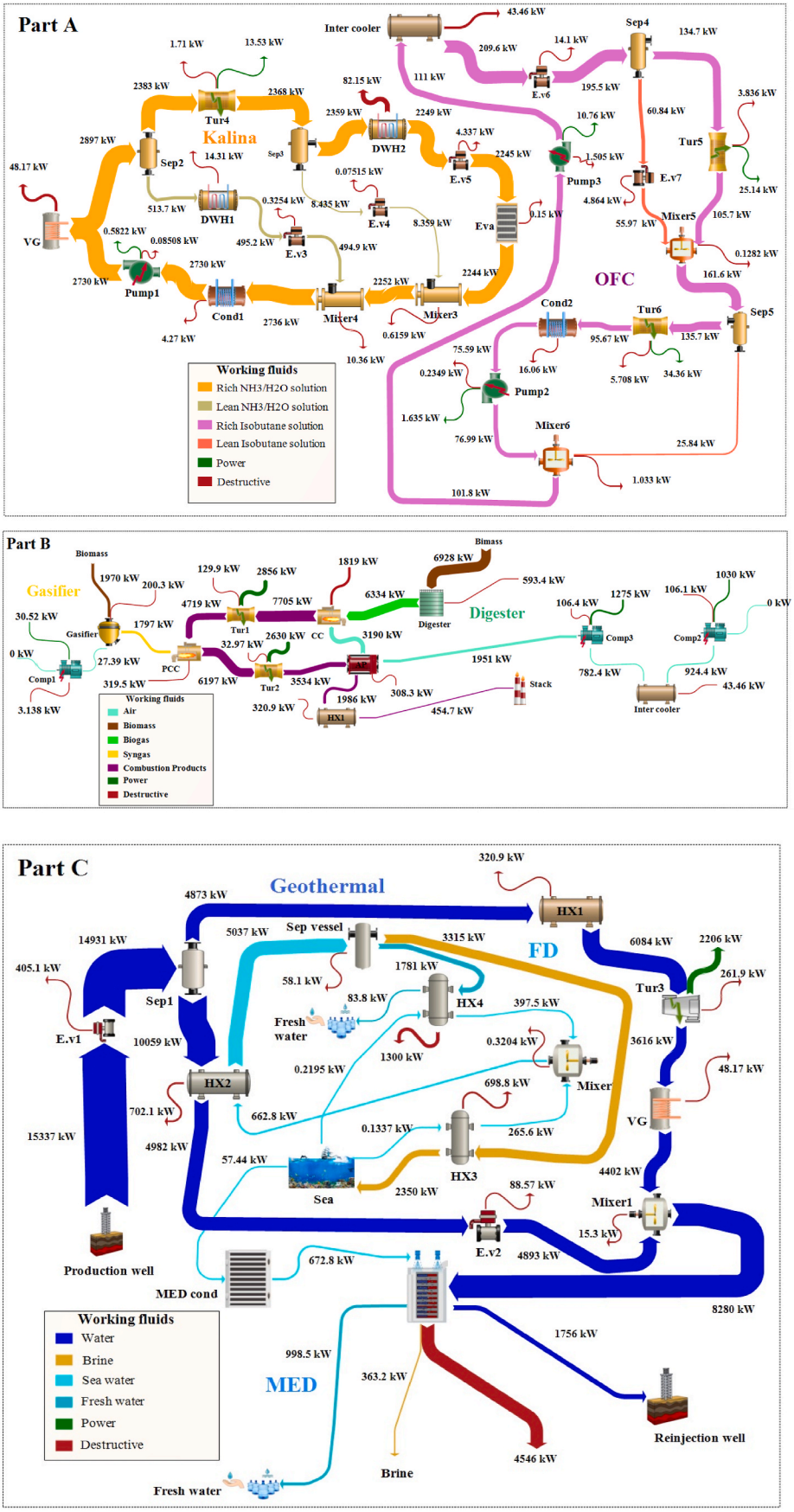

Fig. 5. (Parts A, B, C). The Sankey diagram corresponding to each segment of the suggested system.

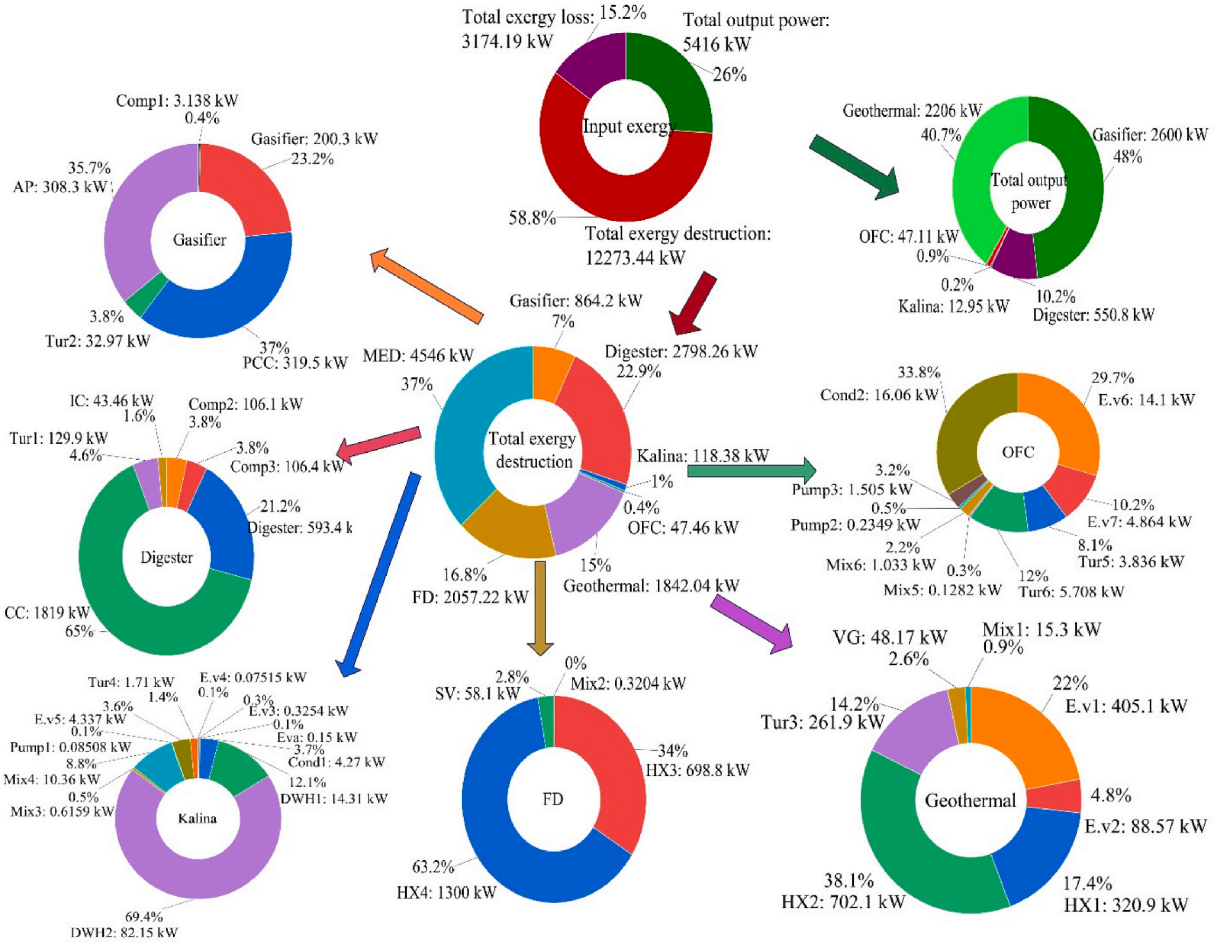

Fig. 6. The pie chart of the exergy destruction percentage for the components of the multi-generation system.

are calculated as [33]:

$$r_k = \frac{c_{P,k} - c_{F,k}}{c_{F,k}} \tag{58}$$

$$f_k = \frac{\dot{Z}_k}{\dot{Z}_k + c_{F,k}\left(\dot{E}_{D,k} + \dot{E}_{L,k}\right)} \tag{59}$$

The implementation of these economic analysis to the system components is elaborated in Table S2 of supplementary file [24,26,30,33].

3.4.1. Total capital investment

Table S3 of supplementary file [33] outlines the key elements for estimating the total capital investment (TCI) of the proposed power generation system. The cost estimation for fixed investment involves two main categories: direct and indirect costs. Other costs are excluded from the study, and the total investment is calculated based on these direct and indirect costs [33]:

$$TCI = FCI + other\ outlays = DC + IC \tag{60}$$

3.5. Economic analysis

Before investing in a project, it is important to estimate the potential profit. The net present value (NPV) method is used in the present work to assess the economic feasibility of the proposed system. The net cash flow at the end of each year is converted into present value using the interest rate [33]:

$$NPV_{bl} = -TCI + \sum_{bl=0}^{bl} Y\ IF_{bl}\ RDF_{bl} \tag{61}$$

Here, i is the interest rate, which is assumed to be 15 %, bl is the economic life of the proposed plant, which is assumed to be 20 years, IF_{bl} is Interest Factor for baseline period and RDF_{bl} is Recovery Discount Factor for baseline period. Furthermore, Y represents the net cash flow at the end of year bl, which is given as [26,33]:

$$Y = AI - \left(C^{O\&M} + C_f\right) \tag{62}$$

AI is annual income, $C^{O\&M}$ is operating and maintenance costs, and C_f is fuel cost. These terms are defined as follows:

$$AI = c_{elec} \times N \times \dot{W}_{net} + c_{fw} \times N \times V_{fw} + c_{Heat} \times N \times \dot{Q}_{Heat} + c_{Cool} \times N \times \dot{Q}_{Cool} \tag{63}$$

$$C^{O\&M} = 0,06 \times PEC \tag{64}$$

$$C_f = \dot{C}_6 + \dot{C}_{11} + \dot{C}_{17} \tag{65}$$

$$IF_{bl} = \left(1 + \left(\frac{i}{100}\right)\right)^{-bl} \tag{66}$$

$$RDF_{bl} = \left(1 + \left(\frac{Ri}{100}\right)\right)^{-bl} \tag{67}$$

The payback period (PBP) is the minimum time needed for the

Table 8
Results of exergy-economic analysis of multi-generation system components.

Component	$\dot{E}x_F$ [kW]	$\dot{E}x_P$ [kW]	$\dot{E}x_D$ [kW]	ε [%]	f_k [%]	r_k [%]
Digestion						
Comp2	1030	924.4	106.1	89.71	48.75	22.38
Comp3	1275	1169	106.4	91.66	48.68	17.73
Digester	6928	6334	593.4	91.43	21.41	11.92
CC	9524	7705	1819	80.9	3.593	24.48
Tur1	2986	2856	129.9	95.65	68.28	14.34
IC	142.1	98.6	43.46	69.4	11.8	49.98
Gasification						
Comp1	30.52	27.39	3.138	89.72	48.94	22.44
Gasifier	1997	1797	200.3	89.97	70.89	27.68
PCC	6516	6197	319.5	95.1	7.263	5.56
Tur2	2663	2630	32.97	98.76	82.63	7.216
AP	1547	1239	308.3	80.07	46.8	46.78
Geothermal cycle						
E.V1	15337	14931	405.1	97.36	39.57	6.733
E.V2	4982	4893	88.57	98.22	72.96	12.63
Sep1	14931	14931	0	100	–	–
HX1	1532	1211	320.9	79.05	10.29	27.61
HX2	5077	4375	702.1	86.17	71.67	36.16
Tur3	2467	2206	261.9	89.39	96.98	79.71
VG	214.3	166.1	48.17	77.52	32.74	43.11
Mix1	8295	8280	15.3	99.82	–	–
Kalina cycle						
Sep2	2897	2897	0	100	–	–
Sep3	2368	2368	0	100	–	–
E.V3	495.2	494.9	0.3254	99.93	28.33	0.09173
E.V4	8.435	8.359	0.07515	99.11	2.927	0.9261
E.V5	2249	2245	4.337	99.81	2.657	0.1985
DWH1	18.51	4.196	14.31	22.67	18.17	80.65
DWH2	109.8	27.66	82.15	25.19	13.37	77.42
Mix3	2252	2252	0.6159	99.97	–	–
Mix4	2747	2736	10.36	99.62	–	–
Eva	1.032	0.8822	0.15	85.47	98.9	93.91
Cond1	6.264	1.994	4.27	31.83	76.91	90.27
Tur4	15.24	13.53	1.71	88.87	98.81	91.39
Pump1	0.5822	0.4971	0.08508	85.39	65.3	49.32
Organic Flash Cycle (OFC)						
E.V6	209.6	195.5	14.1	93.27	1.201	7.298
E.V7	60.84	55.97	4.864	92	1.337	8.808
Sep4	195.5	195.5	0	100	–	–
Sep5	161.6	161.6	0	100	–	–
Tur5	28.97	25.14	3.836	86.76	90.35	61.26
Tur6	40.07	34.36	5.708	85.75	88.36	58.81
Mix5	161.7	161.6	0.1282	99.92	–	–
Mix6	102.8	101.8	1.033	99	–	–
Pump2	1.635	1.4	0.2349	85.63	40.42	28.17
Pump3	10.76	9.251	1.505	86.01	14.36	18.99
Cond2	20.08	4.025	16.06	20.04	21.05	83.48
Flash Desalination (FD)						
Mix2	663.1	662.8	0.3204	99.95	–	–
HX3	964.2	265.5	698.8	27.53	15.22	75.64
HX4	1697	397.3	1300	23.41	10.66	78.55
SV	5295	5037	58.1	98.86	–	–
Multi-Effect Desalination (MED)						
MED	6581	2035	4546	30.92	43.33	74.74

project's NPV to become positive. The PBP of the reference system is the time required for the NPV to exceed zero [33].

$$PBP = min\{bl : NPV(bl) > 0\} \tag{68}$$

3.6. Performace criteria

The system exergy efficiency is calculated as:

$$(\eta_{II})_{total} = \frac{\dot{W}_{net,Total} + (\dot{E}_{61} - \dot{E}_{60}) + (\dot{E}_{63} - \dot{E}_{62}) + (\dot{E}_{65} - \dot{E}_{64}) + \dot{E}_{40} + \dot{E}_{35} + \dot{E}_{39}}{\dot{E}_{fuel,dig} + \dot{E}_{11} + \dot{E}_{38} + \dot{E}_{28} + \dot{E}_{30} + (\dot{E}_{17} - \dot{E}_{27})} \tag{69}$$

The sum unit cost of product for the multi-generation system is also defined as:

$$C_{p,total} = \frac{\dot{C}_{w,total} + (\dot{C}_{61} - \dot{C}_{60}) + (\dot{C}_{63} - \dot{C}_{62}) + (\dot{C}_{65} - \dot{C}_{64}) + \dot{C}_{40} + \dot{C}_{35} + \dot{C}_{39}}{\dot{W}_{net,total} + (\dot{E}_{61} - \dot{E}_{60}) + (\dot{E}_{63} - \dot{E}_{62}) + (\dot{E}_{65} - \dot{E}_{64}) + \dot{E}_{40} + \dot{E}_{35} + \dot{E}_{39}} \tag{70}$$

To determine the effectiveness of multi-effect desalination system, the followings are defined and calculated:

The gain output ratio (GOR) represents the ratio of the freshwater production rate to the input heating steam flow rate [40]:

$$GOR = \frac{\dot{m}_{fw}}{\dot{M}_{HS}} \tag{71}$$

In the above relationship, $\dot{m}_{fw}$ denotes mass flow rate of freshwater and $\dot{M}_{HS}$ indicates the heating steam flow rate.

The recovery ratio (RR) is a key performance indicator in desalina-

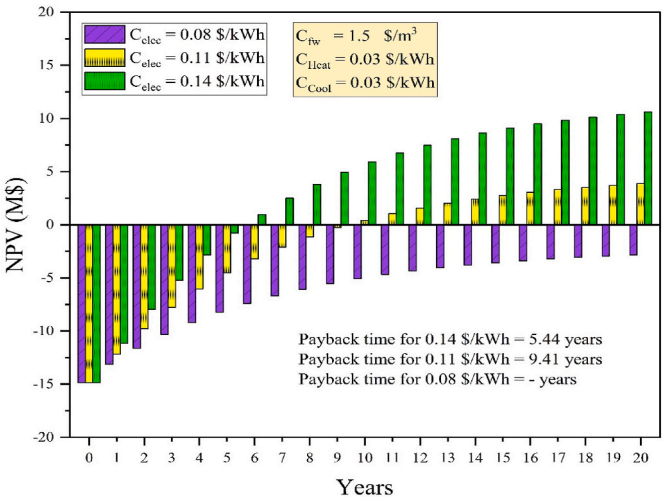

Fig. 7. The assessment of the PP and NPV criteria for various costs.

tion process, showing the percentage of feedwater converted into freshwater [40]:

$$RR = \frac{\dot{m}_{fw}}{\dot{m}_{feedwater}} \tag{72}$$

Here, $\dot{m}_{fw}$ denotes mass flow rate of freshwater and $\dot{m}_{feedwater}$ is mass flow rate of feedwater.

The specific heat transfer area (SHTA) represents the amount of heat transfer surface area needed to produce 1 kg of freshwater [40].

$$SHTA = \frac{A_{tot,MED}}{\dot{m}_{fw}} \tag{73}$$

Where, $A_{tot,MED}$ is total area of the desalination plant and $\dot{m}_{fw}$ denotes mass flow rate of freshwater.

3.7. Multi-objective optimization

The Gray Wolf Optimization (GWO) algorithm, introduced by Mir

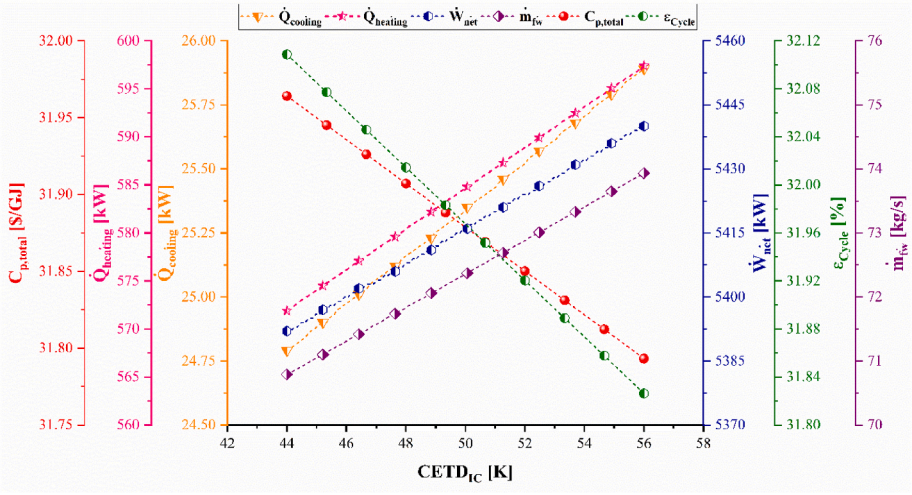

Fig. 8. The variation of the cold-end temperature difference of the intercooler.

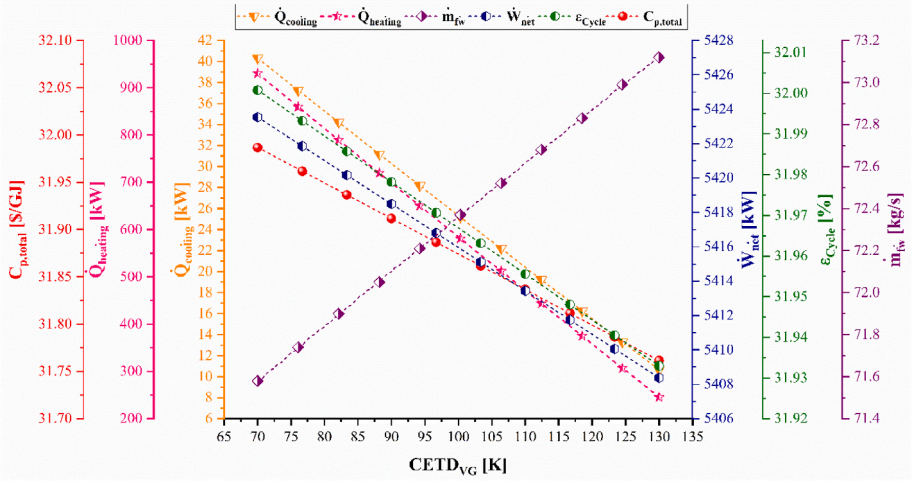

Fig. 9. The variation of the cold-end temperature difference of the vapor generator.

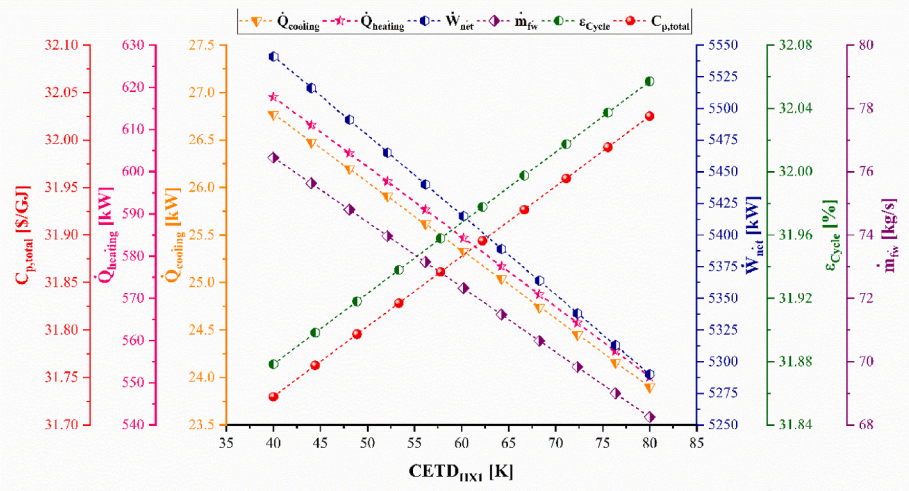

Fig. 10. The variation of the cold-end temperature difference of Heat Exchanger 1.

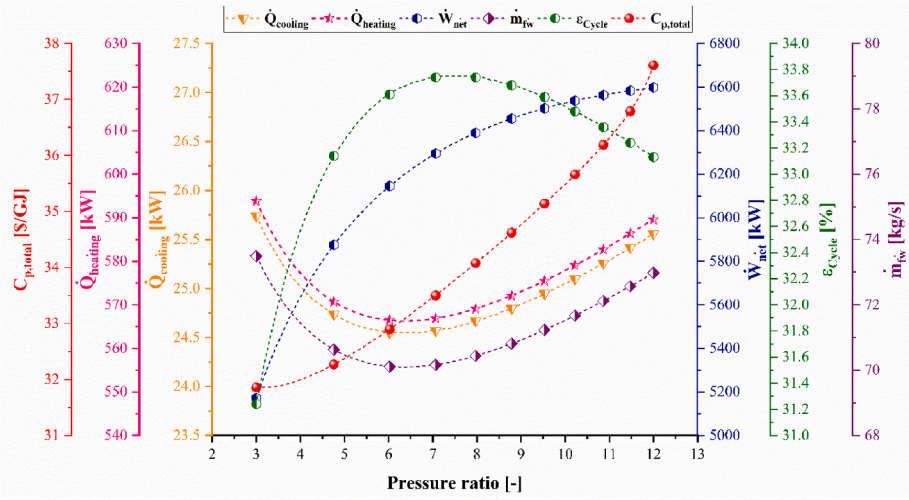

Fig. 11. The variation of the pressure ratio of the compressors and turbines.

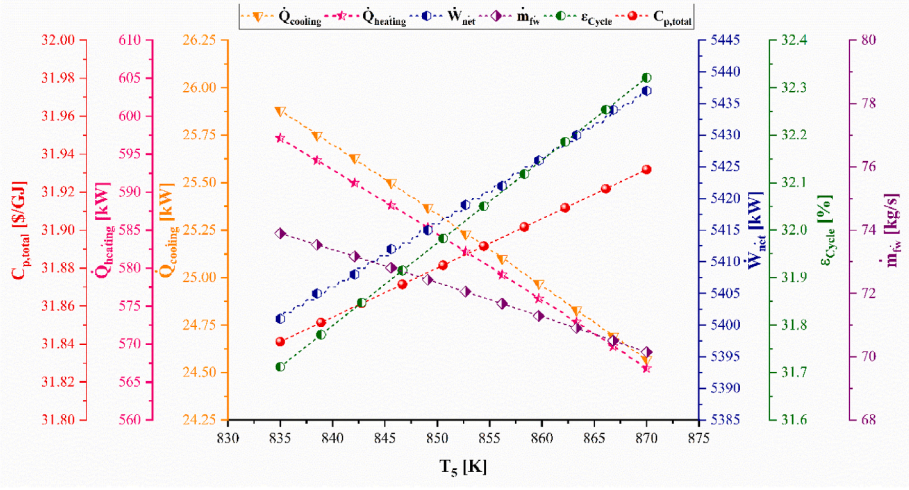

Fig. 12. The variation of the inlet air temperature to the combustion chamber.

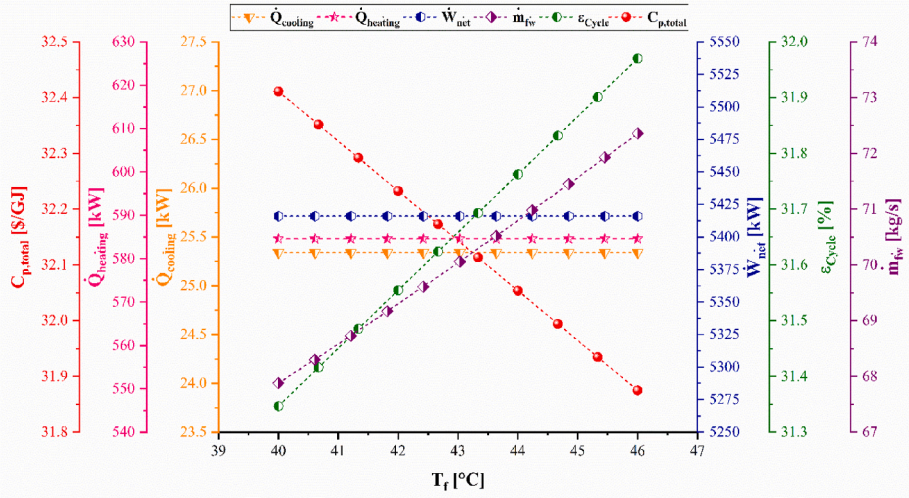

Fig. 13. The variation of the feedwater temperature entering the multi-effect desalination system.

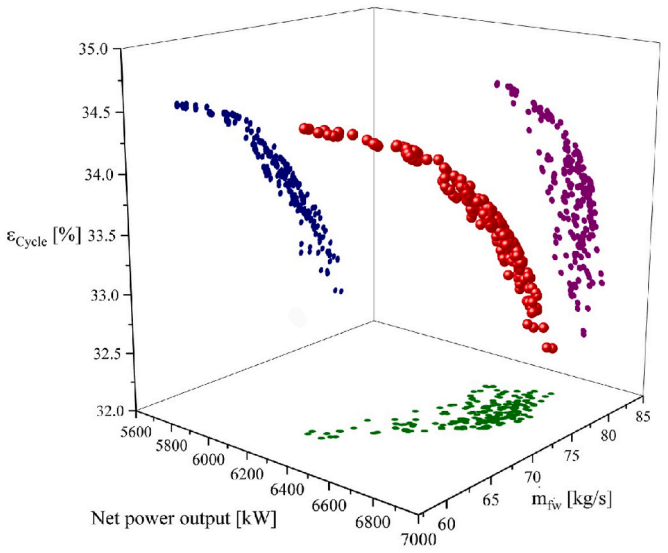

Fig. 14. The Pareto front diagram for the first scenario.

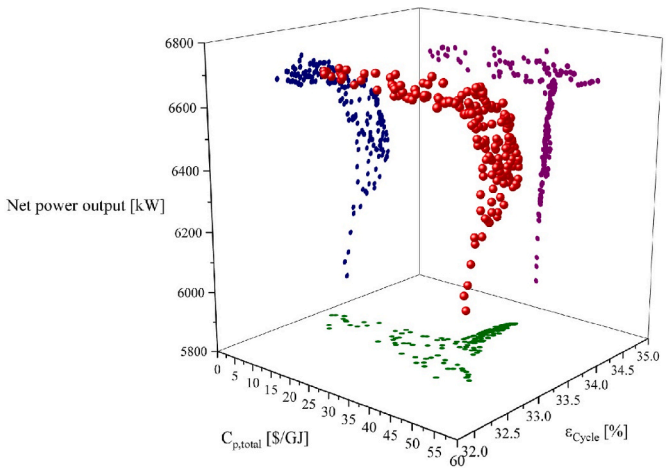

Fig. 15. The Pareto front diagram for the second scenario.

Jalali et al. [41] in 2014, is inspired by the social behavior and group hunting strategies of gray wolves to solve complex optimization problems. With multi-objective optimization, GWO is enhanced by incorporating Pareto front concepts. Each solution (wolf) has an objective function vector to evaluate performance across multiple objectives. Solutions are ranked, with non-dominated solutions placed in the first front. The top three wolves guide the rest, simulating hunting behavior to locate the optimal solution [41,42]:

$$\vec{D}_{\alpha} = \left| \vec{C}_1 \bullet \vec{X}_{\alpha}(t) - \vec{X} \right| \tag{74}$$

$$\vec{D}_{\beta} = \left| \vec{C}_2 \bullet \vec{X}_{\beta}(t) - \vec{X} \right| \tag{75}$$

$$\vec{D}_{\delta} = \left| \vec{C}_3 \bullet \vec{X}_{\delta}(t) - \vec{X} \right| \tag{76}$$

$$\vec{X}_1 = \vec{X}_{\alpha} - \vec{A}_1 \bullet \vec{D}_{\alpha} \tag{77}$$

$$\vec{X}_2 = \vec{X}_{\beta} - \vec{A}_2 \bullet \vec{D}_{\beta} \tag{78}$$

$$\vec{X}_3 = \vec{X}_{\delta} - \vec{A}_3 \bullet \vec{D}_{\delta} \tag{79}$$

$$\vec{X}(t+1) = \left(\vec{X}_1 + \vec{X}_2 + \vec{X}_3 \right) \Big/ 3 \tag{80}$$

Here, t is the current iterations, $\vec{X}$ is the gray wolf's position vector and $\vec{A}$, $\vec{C}$ are coefficient vectors.

An external Pareto archive stores the optimal non-dominated solutions, with the best values of α, β, and δ selected through a leading approach. To ensure diversity, the crowding distance concept is used, helping to distribute solutions uniformly across the objective space. Two multi-objective optimization scenarios are applied.

1. The first case optimizes second law efficiency, generated power, and produced freshwater.
2. The second case optimizes second law efficiency, generated power, and sum unit cost of product.

The MOGWO method requires decision-making parameters, with decision variables listed in Table 2.

Fig. 2 presents a general flowchart of the works done for the article. The process begins with analyzing the multi-generation system from

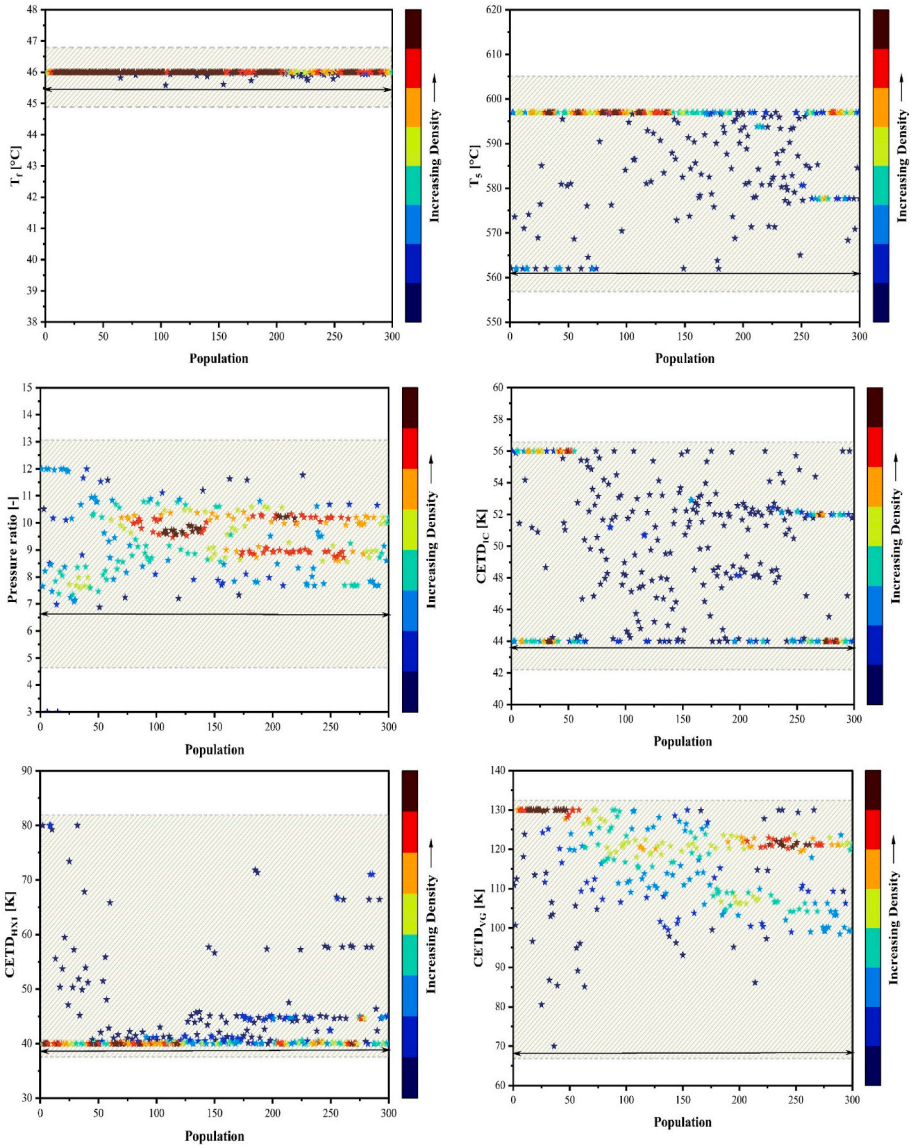

Fig. 16. Scatter distribution for the decision variables for the first scenario.

energy, exergy, and economic perspectives. Next, a parametric study is conducted, followed by system optimization using MATLAB software.

4. Validation

To validate the gasifier's performance, results from this research are compared with those reported by Loha et al. [43,44] including both the experimental and simulation ones. Fig. 3 shows that the mole fraction values of hydrogen, carbon monoxide, carbon dioxide, and methane obtained in the present work are closer to experimental values compared to the simulation values of Loha et al. [43,44].

Table 3 validates the Kalina cycle results using the work done by Du et al. [45], which used a radial turbine with an inlet temperature of 393.20 K, an inlet pressure of 3352 kPa, and a mass flow rate of 2.083 kg/s. The turbine generated an output power of 199.440 kW, an energy efficiency of 8.312 %, and an exergy efficiency of 31.261 %. The relative difference was less than 0.024 %.

Table 4 validates the model used for the Multi-Effect Desalination (MED) system making use of the study by Abdelhay et al. [40]. With 8 desalination stages and parameters including a hot water temperature of 69 °C, inlet brine temperature of 25 °C, seawater salinity of 35 g/kg, final stage salinity of 70 g/kg, freshwater production rate of 6.366 kg/s, inlet feedwater temperature of 35 °C, and final stage temperature of 38.78 °C. The relative differences were found to be less than 6.75 %.

The simulated geothermal power plant in this research is a binary flash type. Two validations were conducted: the first one, comparing the results with the study reported in paper [46], is presented in Tables 5 and 6. Fig. 4 shows the validation of geothermal power plant with results from Li et al. [47]. In the second validation, shown in Fig. 4, compares the simulated steam turbine output power at different flash pressures with results from Li et al. [47].

5. Results

The results from the employed approaches, including comparative analysis, parametric studies, optimization outcomes, and analyses in base-mode operation are presented here. The results are carefully organized into distinct subsections for thorough examination.

5.1. Base-mode results

This section establishes the system performance under regular

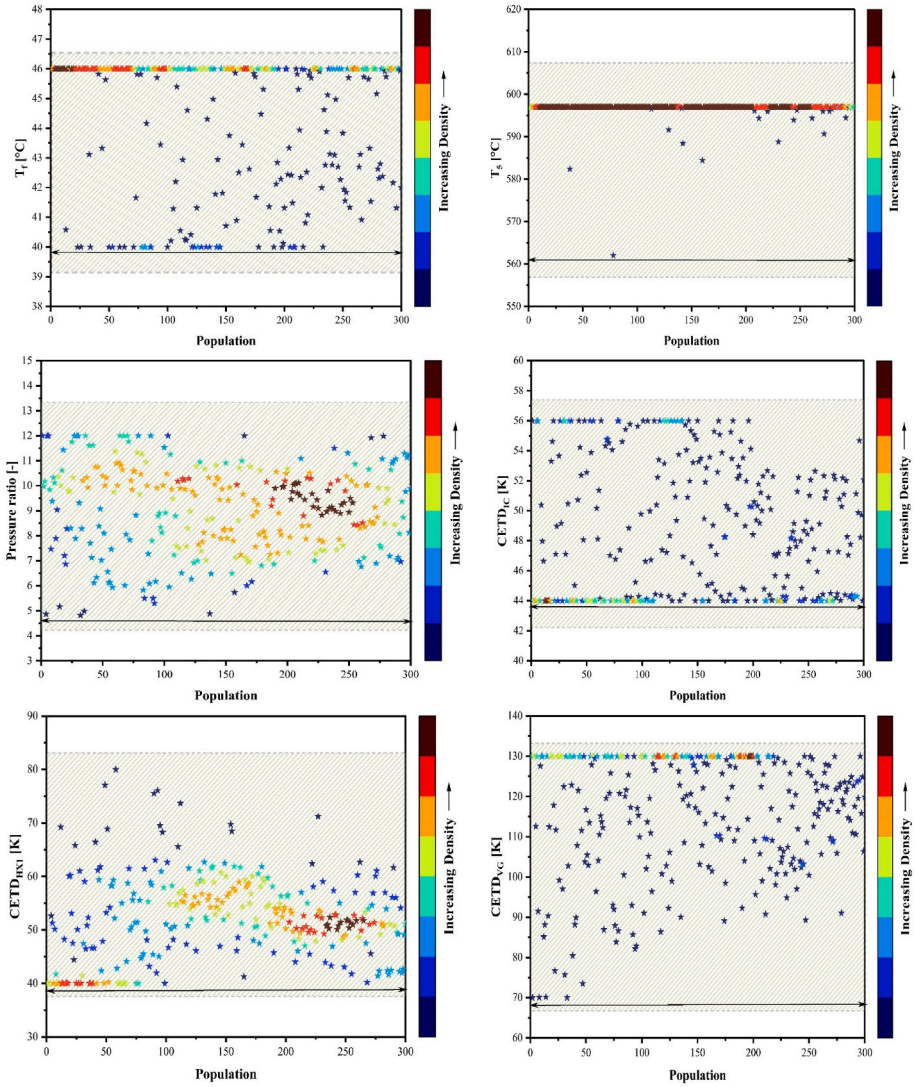

Fig. 17. Scatter distribution for the decision variables for the second scenario.

operating settings, referred to as the base mode.

5.1.1. *Thermodynamic analysis*

Table 7 provides detailed information on the streams in the proposed system. It includs essential elements such as working fluid, temperature, pressure, concentration, mass flow rate, exergy rate, and cost per unit of exergy. These data serve as a fundamental basis for the thermodynamic and economic studies conducted, offering a comprehensive overview of each stream's operational attributes. The table content enhances understanding of the system's overall dynamics and efficiency, making it crucial for a thorough evaluation from both thermodynamic and economic perspectives.

Fig. 5 (Parts A, B, C) presents the Sankey diagram for the multi-generation system, illustrating the input exergy, output exergy, exergy destruction, and power production for each component.

Fig. 6 provides a clearer understanding of the exergy destruction throughout the entire system, as well as the exergy loss and power production of each subsystem.

The total power production is 5416 kW, representing 26 % of the total input exergy, while the total destroyed exergy is 12,273.44 kW (58.8 %), and lost exergy amounts to 3174.19 kW (15.2 %).

Refering to Fig. 6, the GT cycle (Tur2) generates the most power at 2600 kW (48 %), followed by the geothermal subsystem at 2206 kW (40.7 %), the digester (Tur1) at 550.8 kW (10.2 %), the organic flash cycle at 47.11 kW (0.9 %), and the Kalina subsystem at 12.95 kW (0.2 %).

In terms of exergy destruction, the multi-effect desalination (MED) subsystem has the highest portion, at 4546 kW (37 %), followed by the digester at 2798.26 kW (22.9 %) and the flash desalination subsystem at 2057.22 kW (16.8 %). Other subsystems include geothermal (1842.04 kW, 15 %), gasifier (864.2 kW, 7 %), Kalina (118.38 kW, 1 %), and organic flash (47.46 kW, 0.4 %).

Key exergy destruction and the percentage of each exergy destruction of each sub system detail in the subsystems include.

- Digester: Combustion chamber (1819 kW, 65 %) and digester (593.4 kW, 21.2 %).
- Flash desalination: Heat Exchanger 4 (1300 kW, 63.2 %) and Heat Exchanger 3 (698.8 kW, 34 %).
- Geothermal: Heat Exchanger 2 (702.1 kW, 38.1 %) and throttling valve 1 (405.1 kW, 22 %).
- Gasifier: Post-combustion chamber (319.5 kW, 37 %) and air preheater (308.3 kW, 35.7 %).
- Kalina cycle: Domestic Water Heater 2 (82.15 kW, 69.4 %) and Domestic Water Heater 1 (14.31 kW, 12.1 %).
- Organic flash cycle: Condenser 2 (16.06 kW, 33.8 %) and Throttling Valve 6 (14.1 kW, 29.7 %).

The findings from the study of the multi-generation system components, including fuel exergy, product exergy, exergy destruction, exergy efficiency, relative cost difference, and exergy-economic factor, are summarized in Table 8.

5.1.2. Economic analysis

To calculate the payback period, three electricity selling price at \$0.08, \$0.11, and \$0.14/kWh are considered. Fig. 7 indicates the assessment of the PP and NPV criteria for various costs. As shown in Fig. 7, with a freshwater selling price of \$1.5/m^3 and heating/cooling of \$0.03/kWh, the variation in payback period with electricity price is as follows. At 0.08 \$/kWh, the multi-generation system will not achieve profitability in 20 years. At \$ 0.11/kWh, it will become profitable after 9.41 years, and at \$ 0.14/kWh, profitability will begin after 5.44 years. The initial fixed investment cost is 14.88 M\$.

So increasing the electricity sale price improves the system's profitability and shortens the payback period as expected. The economic analysis highlights how pricing strategies for selling electricity can significantly impact the overall economic performance of the system.

5.1.3. The overall results

The comprehensive thermodynamic and economic studies conducted under baseline conditions yield significant findings about the system's performance. The key performance metrics for the multi-generation system include a fuel exergy of 22,535.21 kW, a product exergy of 7203.77 kW, and a destroyed exergy of 12,273.44 kW, resulting in a second law efficiency of 31.97 %. The system achieves a net power output of 5416 kW, along with heating and cooling rates of 584.6 kW and 25.34 kW, respectively. Additionally, the mass flow rate of produced freshwater is 72.36 kg/s, and the unit exergy cost of total products is 31.88 \$/GJ. For the multi-effect desalination (MED) system, the analysis indicates a specific heat transfer area (SHTA) of 117.7 m^2/kg/s, a recovery ratio (RR) of 40 %, and a gain output ratio (GOR) of 3.701.

The results illustrate the system's proficiency in effectively generating electricity, heating, cooling, and freshwater, while also identifying areas of energy loss, specifically with exergy destruction and losses.

5.2. Parametric study

This section presents a parametric analysis to evaluate how key performance criteria affect the overall performance of the proposed system. The selected variables include the cold-end temperature differences of the intercooler, VG, and HX1, as well as the pressure ratio, inlet air temperature for the combustion chamber, and the saline feedwater temperature. Performance criteria analyzed include net generated electricity, freshwater production rates, unit exergy cost of total products, exergy efficiency, heating rate, and cooling rate.

5.2.1. The cold-end temperature difference of the intercooler

Fig. 8 illustrates the impact of the cold-end temperature difference of the intercooler ($CETD_{IC}$) on several performance factors of the system. As $CETD_{IC}$ increases, the freshwater production, power generation, heating, and cooling rates all rise, while the second law efficiency declines. This is primarily due to an increase in the inlet temperature to compressor 3 (T_3), leading to greater power consumption and higher heat loss for the geothermal cycle. This raises the mass flow rates in both the geothermal and Kalina cycles, boosting power generation and thermal output. However, the energy content for the organic flash cycle decreases, reducing its power generation slightly, though this effect is negligible compared to contributions of the geothermal and Kalina cycles.

As a result, the total power generation increases from 5392 to 5440 kW, the heating rate grows from 571.9 to 597.4 kW, the cooling rate from 24.79 to 25.89 kW, and freshwater production rises from 70.79 to 73.93 kg/s. The second law efficiency decreases from 32.11 % to 31.83 % due to the higher geothermal mass flow rate. Despite the drop in exergy efficiency, the unit exergy cost of the total products falls slightly from 31.96 to 31.79 \$/GJ.

5.2.2. The cold-end temperature difference of the VG

Fig. 9 examines the effects of varying the cold-end temperature difference of the vapor generator ($CETD_{VG}$) from 70 to 130° on system performance. As $CETD_{VG}$ increases, the heat load entering the Kalina cycle is reduced, resulting in a lower mass flow rate, which in turn decreases power generation, cooling rate, and heating rate. Despite the Kalina cycle's relatively minor contribution to total power, this reduction lowers second law efficiency and the unit exergy cost of the total products. However, the higher $CETD_{VG}$ raises the outlet temperature of the geothermal working fluid (T_{22}), increasing heat input to the multi-effect desalination cycle and boosting freshwater production.

The results indicate a slight decline in power generation from 5424 to 5408 kW, a reduction in the heating rate from 930.5 to 924.4 kW, and a significant drop in the cooling rate from 40.33 to 10.64 kW. Second law efficiency decreases from 32 % to 31.93 %, and the unit exergy cost of total products decreases from 31.98/GJ to 31.75 \$/GJ. Freshwater production, however, increases from 71.58 to 73.12 kg/s due to the higher heat input to the desalination cycle.

5.2.3. The cold-end temperature difference of HX1

Fig. 10 shows the impact of the cold-end temperature difference of the Heat Exchanger 1 (HX1) on several performance factors of the system. Refering to Fig. 10, the effects of cold-end temperature difference in Heat Exchanger 1 on system performance are studied. As the temperature difference increases, the generated power decreases due to reduced mass flow rate in both the geothermal and Kalina cycles, leading to lower outputs from turbines 3 and 4. This also reduces heating, cooling rates, and freshwater production. While the second law efficiency slightly improves from 31.88 % to 32.06 % because of a decrease in geothermal cycle mass flow rate, the unit exergy cost rises from 31.73 to 32.02 \$/GJ. Power generation falls from 5541 kW to 5290 kW, heating rate from 617.7 kW to 551.4 kW, cooling rate from 26.77 kW to 23.9 kW, and freshwater production from 76.45 kg/s to 68.25 kg/s.

5.2.4. The pressure ratio

Fig. 11 indicates the impact of the pressure ratio of the compressors and turbines on several performance factors of the system. Referring to Fig. 11, as the pressure ratio of compressors and turbines increases from 3 to 12, the power output of all turbines rises, leading to an overall power generation increase from 5772 kW to 6638 kW. The input heat to the geothermal and Kalina cycles first decreases and then increases, causing minimum values for these parameters. The heating rate changes from 593.8 kW to 589.6 kW, with a minimum value of 566.3 kW, while the cooling rate varies from 25.74 kW to 26.56 kW, with a minimum value of 24.55 kW. Freshwater production follows the same trend, ranging from 73.49 kg/s to 72.98 kg/s, with a minimum value of 70.09 kg/s. The second law efficiency peaks at 33.75 % at a pressure ratio of 7 before decreasing. As power generation increases, the unit exergy cost of the products also rises, increasing from 31.86 to 37.61 \$/GJ.

5.2.5. The air temperature entering the combustion chamber

Fig. 12 shows the impact of the inlet air temperature to the combustion chamber on several performance factors of the system. According to Fig. 12, as the air temperature entering the combustion chamber (T_5) increases from 835 to 870 K, the heat transfer in the air preheater rises, which reduces the input heat to the geothermal cycle through Heat Exchanger 1. This reduction leads to a decreased mass flow rate and output power of turbine 3, while the Kalina cycle also experiences a reduced mass flow rate, resulting in a lower power output from Turbine 4 and decreased heating and cooling rates. Freshwater production diminishes as well. However, the increased inlet air temperature boosts the power output of Turbine 1 and, due to the afterburner, also raises Turbine 2's output, leading to an overall increase in the total

power generation from 5401 kW to 5437 kW. This results in an improvement in the second law efficiency from 31.72 % to 32.33 %. The unit exergy cost of total products increases from 31.84 to 31.93 $/GJ, while the heating rate decreases from 597.2 kW to 567 kW, the cooling rate is reduced from 25.88 kW to 24.58 kW, and the freshwater production mass flow rate is decreased from 73.91 kg/s to 70.18 kg/s.

5.2.6. The saline feedwater temperature

Fig. 13 indicates the impact of the feedwater temperature entering the multi-effect desalination system on several performance factors of the system. As Fig. 13 indicates the change in the feedwater temperature entering the multi-effect desalination system from 40 to 46 °C significantly affects freshwater production, while power generation, heating rate, and cooling rate remain constant at 5416 kW, 584.6 kW, and 25.34 kW, respectively. The increase in feedwater temperature reduces the heat required for evaporation and leads to an increase in the freshwater production mass flow rate from 67.88 kg/s to 72.36 kg/s. Consequently, the second law efficiency rises from 31.34 % to 31.97 %, and the unit exergy cost of total products decreases from 32.41 to 31.88 $/GJ. This highlights the importance of feedwater temperature changes in optimizing the desalination subsystems in the multi-generation system.

5.3. Optimization

This section presents the results of the multi-objective optimization using the Multi-Objective Gray Wolf Optimizer (MOGWO) method. More attention is paid to key decision variables such as the cold-end temperature differences of the intercooler (IC), of VG, and of heat exchanger 1 (HX1), along with the pressure ratio of turbines and compressors, inlet air temperature to the combustion chamber, and feedwater temperature for the multi-effect desalination system. The optimization is conducted under two scenarios, with Figs. 14 and 15 illustrating the Pareto frontier generated by the MOGWO method. The LINMAP technique is then applied to identify the most optimal solution from this frontier.

Fig. 14 presents the optimization results for the first scenario, identifying 33.54 % exergy efficiency, a net power output of 6538 kW, and a freshwater production rate of 75.56 kg/s as the optimal solution.

Fig. 15 displays the optimization results for the first scenario, where the optimal solution includes 33.96 % exergy efficiency, a net power output of 6398 kW, and a unit exergy cost of total products at 33.59 $/GJ.

These results summarize the key performance indicators for both scenarios, highlighting variations in exergy efficiency, power generation, freshwater production, and exergo-economic performance.

Scatterplots are used to illustrate the constraints on the optimization method, the convergence of individual variables, and the tested values. Figs. 16 and 17 illustrating the scatter distribution for the decision variables of the system. In the first scenario, as shown in Fig. 16, the optimal feedwater temperature for the multi-effect desalination system is identified as 46 °C due to population clustering at this value. The optimal inlet air temperature to the combustion chamber is 597 °C. The optimal pressure ratios for the compressor and turbine vary within the selected range of 3–12, influenced by clustering in this range. The optimal cold-end temperature difference for the steam generator fluctuates between 120 and 130 K, while for the intercooler, it ranges from 44 to 56 K due to similar clustering. Finally, the optimal cold-end temperature difference for heat exchanger 1 is 40 K.

In the second scenario, as shown in Fig. 17, the optimal feedwater temperature for the multi-effect desalination system remains at 46 °C due to population concentration at this value. The optimal inlet air temperature to the combustion chamber is 597 °C. The pressure ratios for compressors and turbines can vary within the selected range of 3–12, influenced by population clustering. The optimal cold-end temperature difference for the steam generator is 130 K, while the intercooler's optimal range is between 44 and 56 K. Additionally, the optimal cold-end temperature difference for heat exchanger 1 varies from 40 to 60 K.

5.4. Comparative results

Finally, a comparison is made between the exergetic efficiency obtained in the present work and previous studies. This study achieves an exergy efficiency of 31.97 %, significantly higher than the maximum value reported in previous works, including Liu et al. [48] (6.77 %), Kianfard et al. [49] (18.4 %), Abbasi et al. [50] (14.34 %), and Dou et al. [26] (19.61 %). To demonstrate the effectiveness of the proposed system, the optimization results of this study are compared with those reported by Dou et al. [26]. The present study achieves an optimized net power output of 6538 kW, a freshwater production rate of 75.56 kg/s, and an exergy efficiency of 33.54 %. In contrast, the optimized results from Dou et al. [26] show significantly lower values, with a net power output of 836.4 kW, a freshwater production rate of 22.72 kg/s, and an exergy efficiency of 20.55 %. These results highlight the superior performance of the system and its practical potential. Additionally, the environmental sustainability of the system is enhanced which is beneficial for future works. Furthermore, the proposed system is a cost-effective energy use and its environmental impact is low. The above-mentioned advantages of the proposed system make it a promising candidate for further investigation and implementation in future projects.

6. Conclusions

The present paper introduces a multi-generation system integrating a digester and gasifier to enhance efficiency by utilizing two combustion chambers and biomass combustion products. The system channels waste heat from combustion to run the geothermal cycle, whose waste heat is further used to drive a Kalina cycle. Additionally, the geothermal cycle supplies heat to two desalination subsystems: a flash desalination unit and a multi-effect desalination unit. An intercooler is also included to harness heat for an organic flash cycle, generating power. The proposed system produces power, cooling, heating, and freshwater and is evaluated from energy, exergy, and economic perspectives. Optimization is performed using the Gray Wolf Optimizer algorithm in two scenarios.

The results indicate that the overall second law efficiency of the system is 31.97 %, with a total power output of 5416 kW. The overall product unit cost is $31.88/GJ, with a heating rate of 584.6 kW for domestic use and freshwater production of 72.36 kg/s. Considering a selling price of $1.5/m^3 for the produced freshwater and $0.14/kWh for electricity, the payback period is calculated to be 5.44 years.

The highest exergy destruction occurs in the multi-effect desalination subsystem, amounting to 4546 kW, which represents 37 % of the total exergy destruction. The digester ranks second with 2798.26 kW, accounting for 22.9 % of the total. Additionally, variations in the cold-end temperature difference (CETD) of HX1 and the pressure ratio of turbines and compressors significantly influence both exergy efficiency and freshwater production rates. Changes in these parameters directly impact the thermal performance of the system, overall efficiency, and output energy.

For the first optimization scenario, the second law efficiency reaches 33.54 %, with a power output of 6538 kW and freshwater production of 75.56 kg/s. In the second scenario, the second law efficiency increases to 33.96 %, with a power output of 6398 kW and a total unit exergy cost of the products amounting to $33.59/GJ. These findings highlight the potential of the proposed system for sustainable energy and freshwater production.

CRediT authorship contribution statement

Shayan Rabet: Writing – original draft, Visualization, Validation, Software, Resources, Project administration, Methodology, Investigation, Formal analysis, Data curation, Conceptualization. **S.M.S.**

Mahmoudi: Writing – original draft, Visualization, Validation, Software, Resources, Project administration, Methodology, Investigation, Formal analysis, Data curation, Conceptualization. **Mortaza Yari:** Writing – original draft, Visualization, Validation, Software, Resources, Project administration, Methodology, Investigation, Formal analysis, Data curation, Conceptualization. **Saeed Soltani:** Writing – original draft, Visualization, Validation, Supervision, Software, Resources, Project administration, Methodology, Investigation, Formal analysis, Data curation, Conceptualization.

Declaration of competing interest

The authors declare that they have no known competing financial interests or personal relationships that could have appeared to influence the work reported in this paper.

Appendix A. Supplementary data

Supplementary data to this article can be found online at https://doi.org/10.1016/j.renene.2025.122760.

References

[1] C.M. Vivek, P. Ramkumar, P.K. Srividhya, M. Sivasubramanian, Recent strategies and trends in implanting of renewable energy sources for sustainability - a review, Mater. Today Proc. 46 (2021) 8204–8208, https://doi.org/10.1016/j.matpr.2021.03.208.

[2] L.R. Amjith, B. Bavanish, A review on biomass and wind as renewable energy for sustainable environment, Chemosphere 293 (2022) 133579, https://doi.org/10.1016/j.chemosphere.2022.133579.

[3] L.R. Clausen, G. Butera, S.H. Jensen, Integration of anaerobic digestion with thermal gasification and pressurized solid oxide electrolysis cells for high efficiency bio-SNG production, Energy 188 (2019) 116018, https://doi.org/10.1016/j.energy.2019.116018.

[4] S.M. Atnaw, S.A. Sulaiman, L. Singh, Z.A. Wahid, C. Che, K. Yahya, Modeling and parametric study for maximizing heating value of gasification syngas, Bioresources 12 (2017) 2548–2564.

[5] Z.A. Zainal, R. Ali, C.H. Lean, K.N. Seetharamu, Prediction of performance of a downdraft gasifier using equilibrium modeling for different biomass materials, Energy Convers. Manag. 42 (2001) 1499–1515.

[6] K. Arun, M. Venkata Ramanan, S. Sai Ganesh, Stoichiometric equilibrium modeling of corn cob gasification and validation using experimental analysis, Energy & Fuels 30 (2016) 7435–7442.

[7] P. Sittisun, N. Tippayawong, S. Pang, Biomass gasification in a fixed bed downdraft ractor with oxygen enriched air: a modified equilibrium modeling study, Energy Proc. 160 (2019) 317–323, https://doi.org/10.1016/j.egypro.2019.02.163.

[8] M. Ozturk, I. Dincer, Thermodynamic assessment of an integrated solar power tower and coal gasification system for multi-generation purposes, Energy Convers. Manag. 76 (2013) 1061–1072, https://doi.org/10.1016/j.enconman.2013.08.061.

[9] P. Ahmadi, I. Dincer, M.A. Rosen, Development and assessment of an integrated biomass-based multi-generation energy system, Energy 56 (2013) 155–166, https://doi.org/10.1016/j.energy.2013.04.024.

[10] Y. Bicer, I. Dincer, Development of a multigeneration system with underground coal gasification integrated to bitumen extraction applications for oil sands, Energy Convers. Manag. 106 (2015) 235–248, https://doi.org/10.1016/j.enconman.2015.09.020.

[11] S. Khanmohammadi, K. Atashkari, R. Kouhikamali, Modeling and assessment of a biomass gasification integrated system for multigeneration purpose, Int. J. Chem. Eng. 2016 (2016), https://doi.org/10.1155/2016/2639241.

[12] M.H. Taheri, A.H. Mosaffa, L.G. Farshi, Energy, exergy and economic assessments of a novel integrated biomass based multigeneration energy system with hydrogen production and LNG regasification cycle, Energy 125 (2017) 162–177, https://doi.org/10.1016/j.energy.2017.02.124.

[13] S. Balafkandeh, V. Zare, E. Gholamian, Multi-objective optimization of a tri-generation system based on biomass gasification/digestion combined with S-CO2 cycle and absorption chiller, Energy Convers. Manag. 200 (2019) 112057, https://doi.org/10.1016/j.enconman.2019.112057.

[14] W.J. Wujcik, W.J. Jewell, Dry anaerobic fermentation, Biotechnol. Bioeng. Symp. (10) (1980) 43–65.

[15] F. Calise, F.L. Cappiello, L. Cimmino, M. Dentice d'Accadia, M. Vicidomini, A solar-assisted liquefied biomethane production by anaerobic digestion: dynamic simulations for harbors, Renew. Sustain. Energy Rev. 189 (2024), https://doi.org/10.1016/j.rser.2023.114066.

[16] L. Luo, L. Lu, X. Shen, J. Chen, Y. Pan, Y. Wang, et al., Energy, exergy and economic analysis of an integrated ground source heat pump and anaerobic digestion system for Co-generation of heating, cooling and biogas, Energy 282 (2023), https://doi.org/10.1016/j.energy.2023.128220.

[17] C.A. Salman, S. Schwede, M. Naqvi, E. Thorin, J. Yan, Synergistic combination of pyrolysis, anaerobic digestion, and CHP plants, Energy Proc. 158 (2019) 1323–1329, https://doi.org/10.1016/j.egypro.2019.01.326.

[18] A. Baccioli, L. Ferrari, F. Vizza, U. Desideri, Potential energy recovery by integrating an ORC in a biogas plant, Appl. Energy 256 (2019), https://doi.org/10.1016/j.apenergy.2019.113960.

[19] A. Behzadi, E. Houshfar, E. Gholamian, M. Ashjaee, A. Habibollahzade, Multi-criteria optimization and comparative performance analysis of a power plant fed by municipal solid waste using a gasifier or digester, Energy Convers. Manag. 171 (2018) 863–878, https://doi.org/10.1016/j.enconman.2018.06.014.

[20] M. Yari, A.S. Mehr, S.M.S. Mahmoudi, M. Santarelli, A comparative study of two SOFC based cogeneration systems fed by municipal solid waste by means of either the gasifier or digester, Energy 114 (2016) 586–602, https://doi.org/10.1016/j.energy.2016.08.035.

[21] T. Hai, M.A. Ali, A. Alizadeh, S.F. Almojil, A.I. Almohana, A.F. Alali, Reduction in environmental CO2 by utilization of optimized energy scheme for power and fresh water generations based on different uses of biomass energy, Chemosphere 319 (2023), https://doi.org/10.1016/j.chemosphere.2023.137847.

[22] A.H. Mosaffa, A. Zareei, Proposal and thermoeconomic analysis of geothermal flash binary power plants utilizing different types of organic flash cycle, Geothermics 72 (2018) 47–63, https://doi.org/10.1016/j.geothermics.2017.10.011.

[23] Z. Yao, Z. Yuxing, K. Yaqian, B. Sobhani, Research on an integrated power and freshwater generation system from natural gas energy and geothermal sources, Desalination 525 (2022), https://doi.org/10.1016/j.desal.2021.115494.

[24] L. Zhang, B. Sobhani, Comprehensive economic analysis and multi-objective optimization of an integrated power and freshwater generation cycle based on flash-binary geothermal and gas turbine cycles, J. Clean. Prod. 364 (2022), https://doi.org/10.1016/j.jclepro.2022.132644.

[25] F. Hamrang, A. Shokri, S.M. Seyed Mahmoudi, B. Ehghaghi, M.A. Rosen, Performance analysis of a new electricity and freshwater production system based on an integrated gasification combined cycle and multi-effect desalination, Sustain. Times 12 (2020) 1–29, https://doi.org/10.3390/su12197996.

[26] Z. Dou, Y. Zou, A. Mohebbi, Design and multi-aspect analysis of a geothermal and biomass dual-source power , cooling , heating , and hybrid freshwater production system, Energy 293 (2024) 130532, https://doi.org/10.1016/j.energy.2024.130532.

[27] I. Fakhari, A. Behzadi, E. Gholamian, P. Ahmadi, A. Arabkoohsar, Design and tri-objective optimization of a hybrid efficient energy system for tri-generation, based on PEM fuel cell and MED using syngas as a fuel, J. Clean. Prod. 290 (2021), https://doi.org/10.1016/j.jclepro.2020.125205.

[28] H. Nami, S.M.S. Mahmoudi, A. Nemati, Exergy, economic and environmental impact assessment and optimization of a novel cogeneration system including a gas turbine, a supercritical CO2 and an organic Rankine cycle (GT-HRSG/SCO2), Appl. Therm. Eng. 110 (2017) 1315–1330, https://doi.org/10.1016/j.applthermaleng.2016.08.197.

[29] I.S. Al-Mutaz, I. Wazeer, Development of a steady-state mathematical model for MEE-TVC desalination plants, Desalination 351 (2014) 9–18, https://doi.org/10.1016/j.desal.2014.07.018.

[30] Z. Gao, J. Miao, J. Zhao, M. Mesri, Comprehensive economic analysis and multi-objective optimization of an integrated gasification power generation cycle, Process Saf. Environ. Prot. 155 (2021) 61–79, https://doi.org/10.1016/j.psep.2021.09.007.

[31] N. Ghasemzadeh, A. Javaherian, M. Yari, H. Nami, Energy Conversion and Management : X Thermodynamics modelling and optimisation of a biogas fueled decentralised poly-generation system using machine learning techniques, Energy Convers. Manag. X 20 (2023) 100470, https://doi.org/10.1016/j.ecmx.2023.100470.

[32] Laleh S. Sharafi, A. Safarpour, A. Shahbazi Shahrak, S.H. Fatemi Alavi, S. Soltani, Thermodynamic and exergoeconomic analyses of a novel biomass-fired combined cycle with solar energy and hydrogen and freshwater production in sports arenas, Int. J. Hydrogen Energy 59 (2024) 1507–1517, https://doi.org/10.1016/j.ijhydene.2024.02.146.

[33] A. Bejan, G. Tsatsaronis, M.J. Moran, Thermal Design and Optimization, John Wiley & Sons, 1995.

[34] A. Bejan, Advanced Engineering Thermodynamics, John Wiley & Sons, 2016.

[35] F. Hamrang, A. Shokri, S.M.S. Mahmoudi, B. Ehghaghi, M.A. Rosen, Performance analysis of a new electricity and freshwater production system based on an integrated gasification combined cycle and multi-effect desalination, Sustainability 12 (2020), https://doi.org/10.3390/su12197996.

[36] A. Behzadi, E. Houshfar, E. Gholamian, M. Ashjaee, A. Habibollahzade, Multi-criteria optimization and comparative performance analysis of a power plant fed by municipal solid waste using a gasifier or digester, Energy Convers. Manag. 171 (2018) 863–878, https://doi.org/10.1016/j.enconman.2018.06.014.

[37] A. Rosińska, B. Karwowska, Dynamics of changes in coplanar and indicator PCB in sewage sludge during mesophilic methane digestion, J. Hazard Mater. 323 (2017) 341–349, https://doi.org/10.1016/j.jhazmat.2016.04.016.

[38] E. Gholamian, S.M.S. Mahmoudi, V. Zare, Proposal, exergy analysis and optimization of a new biomass-based cogeneration system, Appl. Therm. Eng. 93 (2016) 223–235, https://doi.org/10.1016/j.applthermaleng.2015.09.095.

[39] L. Zhang, B. Sobhani, Comprehensive economic analysis and multi-objective optimization of an integrated power and freshwater generation cycle based on flash-binary geothermal and gas turbine cycles, J. Clean. Prod. 364 (2022) 132644, https://doi.org/10.1016/j.jclepro.2022.132644.

[40] A.O. Abdelhay, H.E.S. Fath, S.A. Nada, Solar driven polygeneration system for power, desalination and cooling, Energy 198 (2020), https://doi.org/10.1016/j.energy.2020.117341.

[41] S. Mirjalili, S. Mohammad, A. Lewis, Grey wolf optimizer, Adv Eng Softw 69 (2014) 46–61, https://doi.org/10.1016/j.advengsoft.2013.12.007.
[42] S.M.S. Mahmoudi, S. Salehi, M. Yari, Three-objective optimization of a novel triple-effect absorption heat transformer combined with a water desalination system, Energy Convers. Manag. 138 (2017) 131–147, https://doi.org/10.1016/j.enconman.2017.01.057.
[43] C. Loha, P. Chatterjee, H. Chattopadhyay, Performance of fluidized bed steam gasification of biomass – modeling and experiment, Energy Convers. Manag. 52 (2011) 1583–1588.
[44] C. Loha, H. Chattopadhyay, P.K. Chatterjee, Thermodynamic analysis of hydrogen rich synthetic gas generation from fluidized bed gasification of rice husk, Energy 36 (2011) 4063–4071, https://doi.org/10.1016/j.energy.2011.04.042.
[45] Y. Du, K. Chen, Y. Dai, A study of the optimal control approach for a Kalina cycle system using a radial-inflow turbine with variable nozzles at off-design conditions, Appl. Therm. Eng. 149 (2019) 1008–1022, https://doi.org/10.1016/j.applthermaleng.2018.12.117.
[46] M. Yari, Exergetic analysis of various types of geothermal power plants, Renew. Energy 35 (2010) 112–121, https://doi.org/10.1016/j.renene.2009.07.023.
[47] J. Li, Z. Ge, Y.-Y. Duan, Z. Yang, Effects of heat source temperature and mixture composition on the combined superiority of dual-pressure evaporation organic Rankine cycle and zeotropic mixtures, Energy 174 (2019), https://doi.org/10.1016/j.energy.2019.02.186.
[48] J. Liu, X. Chen, A. Pugazhendhi, The feasibility of integrating three different thermal desalination units and a geothermal cycle combined with a modified Kalina cycle, Desalination 560 (2023) 116610, https://doi.org/10.1016/j.desal.2023.116610.
[49] H. Kianfard, S. Khalilarya, S. Jafarmadar, Exergy and exergoeconomic evaluation of hydrogen and distilled water production via combination of PEM electrolyzer , RO desalination unit and geothermal driven dual fl uid ORC, Energy Convers. Manag. 177 (2018) 339–349, https://doi.org/10.1016/j.enconman.2018.09.057.
[50] H. Reza, H. Pourrahmani, Multi-objective optimization and exergoeconomic analysis of a continuous solar-driven system with PCM for power , cooling and freshwater production, Energy Convers. Manag. 211 (2020) 112761, https://doi.org/10.1016/j.enconman.2020.112761.